Magneto-optical investigation of complex flux dynamics in superconductors

Atle Jorstad Qviller

Thesis submitted for the degree of Philosophiae Doctor
Department of Physics
University of Oslo
March 14, 2012

Series of dissertations submitted to the
Faculty of Mathematics and Natural Sciences, University of Oslo
No. 1201

ISSN 1501-7710

Cover: Inger Sandved Anfinsen.
Printed in Norway: AIT Oslo AS.

Produced in co-operation with Unipub.
The thesis is produced by Unipub merely in connection with the
thesis defence. Kindly direct all inquiries regarding the thesis to the copyright
holder or the unit which grants the doctorate.

Preface

First, I would like to thank my two experienced supervisors Tom Henning Johansen and Vitaliy Yurchenko for teaching me the science of magneto-optical imaging of superconductors the last four years. This has included defining projects, answering countless questions, giving feedback on publications and spending many hours in the lab. Without all this there would have been no thesis. I would also like to thank Yuri Galperin and Joakim Bergli for sharing their deep theoretical insights during discussions, and Jørn Inge Vestgården for contributing with his unique expertise on simulations of flux dynamics in superconductors. Knut Jørgen Måløy, Arne Skjeltorp and Eirik Grude Flekkøy have provided excellent courses in condensed matter physics and statistical mechanics, this has been very useful for me as a former student of nuclear physics. Assistance with data analysis software from Ken Tore Tallakstad and Olav Aursjø is greatly appreciated. I am also happy to have worked in the lab with Pavlo Mikheenko on advanced superconductors and with Mihailo Jankov on experimental setups. During my stay, members of the AMCS group have provided a friendly and informal attitude facilitating discussions across different fields. Finally, I would like to thank my family for all their support during these years, especially my mother Anne Lise.

Oslo, March 2012
Atle Jorstad Qviller

”Condensed matter physics is the physics of dirt”
- W. Pauli

Overview of the thesis

This work is organized in two parts. In the first part, relevant theory and the used experimental techniques and methods are discussed. In particular, the physics of magneto-optical imaging with in-plane magnetized ferrite garnets and the method of inversion of Biot-Savart's law for deducing two-dimensional current patterns is given a thorough treatment. This material is not new, but at present it is scattered around in many works, meaning that a new researcher in this area will have to read several articles, often with small, but significant differences in physical assumptions and notation. The second part consists of published articles, which form a self-contained presentation of the most important results. A brief summary of the most important results is given, together with perspectives for future researchers on what more could be investigated.

Contents

Part I

Introduction

Chapter 1

Superconductor basics

Many materials become superconducting at cryogenic temperatures including metals, alloys and several cuprates and pnictides. The following chapter gives a brief introduction to the macroscopic phenomena in superconductors of most importance for this work. It roughly follows [1].

1.1 Types of superconductors

A superconductor is characterized by two dramatic macroscopic phenomena: Perfect conductivity and perfect diamagnetism. Below a certain *critical temperature* T_c, electrical resistance disappears, first observed by Kamerlingh-Onnes in 1911. At the same time, any magnetic field present in the specimen is expelled from the superconducting phase. Fields outside the specimen are excluded from entering. This phenomenon of perfect diamagnetism is called *Meissner effect* and was discovered by Meissner and Ochsenfeld in 1933. An illustration of the Meissner effect is shown in Fig. 1.1.

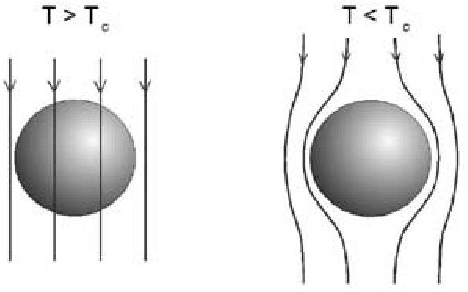

Figure 1.1: Illustration of the Meissner effect.

The perfect diamagnetism cannot be understood from a theory where superconductivity is simply an idealization of classical conductivity. Superconductivity can only be understood as a quantum mechanical phenomenon. Superconductors are classified according to their magnetic and thermodynamical properties as *type-I* or *type-II*.

In a type-I superconductor, the magnetic field is completely expelled until the applied external field H_a reaches the *critical field* H_c. At that point, superconductivity is abruptly destroyed (in samples with a nonzero demagnetization factor, there will however be a complicated pattern of coexistence between normal and superconducting domains). Above the critical field, the magnetization is zero. Below H_c, the superconductor will exhibit perfect diamagnetism with magnetization $M = -H_a$

In contrast, for a type-II superconductor, the magnetic field is only completely expelled up to a value H_{c1}, which is called the *lower critical field*. The superconductivity is, however, not completely destroyed until one reaches the *upper critical field* H_{c2}. Between these two field values, the superconductor is in a *mixed state* or *Shubnikov phase* where the magnetic flux is quantized as *vortices*. Each of these carry the magnetic *flux quantum* $\phi_0 = h/2e = 2.07 \cdot 10^{-15}$ Wb. Superconductivity in a surface layer can exist even further up to a H_{c3}=1.695H_{c2}. Fig. 1.2 schematically show the magnetization of type-I and type-II superconductors.

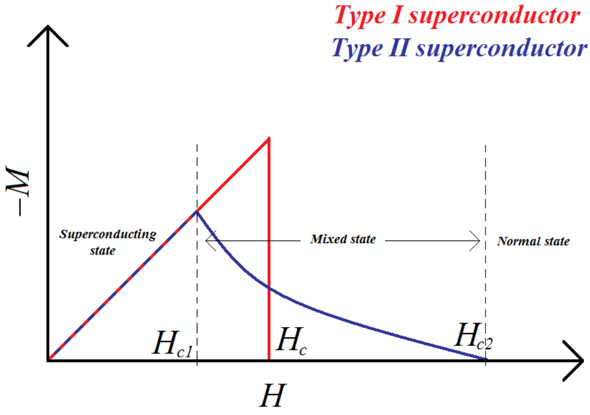

Figure 1.2: Magnetization of type-I and type-II superconductors.

It is an empirical fact that the critical field of the type-I superconductors has a temperature dependence of the following form

$$H_c(T) \approx H_c(0)[1 - (\frac{T}{T_c})^2] \tag{1.1}$$

Most practical applications of superconductivity use type-II materials, which can have very high upper critical fields. All of the high-T_c superconductors are also type-II, though the converse statement is not true.

The microscopic mechanism of most metal and alloy superconductors is well understood and described in the *BCS theory* of 1957 by Bardeen, Cooper and Schrieffer. In this theory, electrons form *Cooper pairs* at low temperatures due to phonon interactions with the crystal lattice. In contrast, there does not exist a satisfactory theory for the microscopic mechanism of the high-temperature superconducting (HTS) materials, although they can still be described by the same macroscopic equations as the superconductors describable by BCS theory. Most evidence points towards purely electronic mechanisms assembling Cooper pairs in these materials, but their complex lattice structures are major obstacles for a reaching a decisive confirmation.

1.2 London theory

In 1935 the London brothers derived two equations governing the electrodynamics of superconductors. The first reads

$$\mathbf{e} = \frac{m^*}{n_s e^{*2}} \cdot \frac{d\mathbf{j}}{dt} \tag{1.2}$$

Local values of E, H and B are denoted with lower case letters. The relationships between these quantities are given by the Maxwell equations

$$\nabla \times \mathbf{e} = -\frac{\partial \mathbf{b}}{\partial t} \tag{1.3}$$

$$\nabla \times \mathbf{h} = \mathbf{j} \tag{1.4}$$

Taking the curl of Eq. (1.2) and combining the resulting equation with Eq. (1.3), Eq. (1.4) and $\mathbf{b} = \mu_0 \mathbf{h}$, one can write

$$\frac{\partial}{\partial t}(\mathbf{b} + \frac{m^*}{\mu_0 n_s e^{*2}} \nabla \times \nabla \times \mathbf{b}) = 0 \tag{1.5}$$

Integrating and setting the integration constant equal to zero, the second London equation results

$$\mathbf{b} + \frac{m^*}{\mu_0 n_s e^{*2}} \nabla \times \nabla \times \mathbf{b} = 0 \tag{1.6}$$

With this choice of integration constant, Eq. (1.6) explains the Meissner effect, as the following derivation will show. Using the vector calculus identity $\nabla \times \nabla \times \mathbf{b} = \nabla(\nabla \cdot \mathbf{b}) - \nabla^2 \mathbf{b}$ and Gauss' law $\nabla \cdot \mathbf{b} = 0$ we can write this as

$$\nabla^2 \mathbf{b} - \frac{\mathbf{b}}{\lambda^2} = 0 \tag{1.7}$$

The last equation contains the *London penetration depth*, given by

$$\lambda = \sqrt{\frac{m^*}{\mu_0 n_s e^{*2}}} \tag{1.8}$$

where m^* is the effective mass of the electron in the medium, n_s is the *number density* of superconducting electrons and $e^* = 2e$ is the charge of a Cooper pair. It becomes obvious why this quantity is called a penetration depth when Eq. (1.7) is solved for the magnitude of $\mathbf{b}$ as a function of x with an applied field given by H_a

$$b(x) = \mu_0 H_a e^{-\frac{x}{\lambda}} \tag{1.9}$$

The magnitude of the field thus decays exponentially with a characteristic length λ, explaining the Meissner effect. There is also another relevant length scale of the superconductor, the *Pippard coherence length*, denoted with ξ_0. It is a measure of the non-locality of the wavefunctions of the superconducting electrons

$$\xi_0 \sim \frac{\hbar v_f}{k_B T_c} \tag{1.10}$$

where v_f is the Fermi velocity of the electron system. The importance of the coherence length and the London penetration depth for the properties of the superconductor will be illuminated in the next section.

1.3 Ginzburg-Landau theory

In 1950, before BCS theory was known, Ginzburg and Landau proposed a macroscopic theory of superconductivity using thermodynamical arguments. This theory is phenomenological, meaning that it does not deal with the microscopic mechanisms behind superconductivity. The theory expands the Helmholtz free energy density f of the superconductor near the transition to the normal state with the aid of an *order parameter* ψ

$$f = f_{n0} + \alpha|\psi|^2 + \frac{\beta}{2}|\psi|^4 + \frac{1}{2m^*}|(-i\hbar\nabla + 2e\mathbf{A})^2\psi|^2 + \frac{1}{2\mu_0}(\nabla \times \mathbf{A}) \tag{1.11}$$

The order parameter is a measure of the density of superconducting electrons

$$n_s = |\psi(x)|^2 \tag{1.12}$$

It is also frequently stated in less formal terms that the order parameter measures how ”deep” the system is into the superconducting state. Without field or gradients, this free energy can be written

$$f_{s0} = f_{n0} + \alpha|\psi|^2 + \frac{\beta}{2}|\psi|^4 \tag{1.13}$$

This equation has a nontrivial minimum at $|\psi|^2 = |\psi_\infty|^2 \equiv -\frac{\alpha}{\beta}$, the value of the order parameter in an infinitely large superconductor. By minimizing the free energy Eq. (1.11) with respect to ψ, one can derive the Ginzburg-Landau equations

$$\frac{1}{2m*}(-i\hbar\nabla + 2e\mathbf{A})^2 + \beta|\psi(x)|^2\psi + \alpha(T)\psi = 0 \tag{1.14}$$

and

$$\mathbf{j} = \frac{i\hbar e}{m^*}(\psi^*\nabla\psi - \psi\nabla\psi^*) - \frac{4e^2}{m^*}|\psi(x)|^2\mathbf{A} \tag{1.15}$$

The first equation Eq. (1.14) looks like the Schrödinger equation for a particle with charge $2e$ and mass m^* in a magnetic field, but has an extra nonlinear term. The second equation Eq. (1.15) describes the supercurrent. A length scale may be defined, the *Ginzburg-Landau coherence length.* At low temperatures, it is approximately equal to the Pippard coherence length ξ_0

$$\xi(T) = \frac{\hbar}{(2m^*|\alpha(T)|)^{1/2}} \tag{1.16}$$

The *Ginzburg-Landau parameter* is defined as the ratio of the two characteristic lengths

$$\kappa = \frac{\lambda}{\xi} \tag{1.17}$$

This parameter classifies the superconductor as type-I ($\kappa < 1/\sqrt{2}$) or type-II ($\kappa > 1/\sqrt{2}$). The penetration depth and the coherence length has approximately the same temperature dependencies, thus making κ approximately constant in temperature. A type-I superconductor has a positive surface energy between normal and superconducting domains of the material, and the phase transition is of first order. In contrast, the surface energy is negative in a type-II material, causing subdivision of the normal state into normal domains of the size of the coherence length, each holding one flux quanta, denoted *vortices* [2]. The phase transition is in this case of second order.

1.4 Structure of a vortex

In a type-II superconductor with a large κ, one can use the London theory to deduce the structure of vortices near H_{c1}, where the density of vortices is small. The magnetic field resulting from a single vortex holding a single flux quantum can be calculated from Eq. (1.7) with a delta function source

$$\mathbf{b} + \lambda^2 \nabla \times \nabla \times \mathbf{b} = \mathbf{i}_z \phi_0 \delta(\mathbf{r}) \tag{1.18}$$

Again using $\nabla \times \nabla \times \mathbf{b} = -\nabla^2 \mathbf{b}$, we find

$$\mathbf{b} - \lambda^2 \nabla^2 \mathbf{b} = \mathbf{i}_z \phi_0 \delta(\mathbf{r}) \tag{1.19}$$

When solved, the radial dependence of the magnitude of $\mathbf{b}$ reads

$$b(r) = \frac{\phi_0}{2\pi\lambda^2} K_0(\frac{r}{\lambda}) \tag{1.20}$$

with K_0 denoting the zeroth order modified Bessel function. It can be approximated to yield expressions in terms of more familiar functions in the limits $\xi \ll r \ll \lambda$ and $\lambda \ll r$. In the first limit, a cutoff has to be done at the coherence length to remove a divergence. The short-distance limit reads

$$b(r) \simeq \frac{\phi_0}{2\pi\lambda^2} (\log \frac{r}{\lambda} + 0.116) \tag{1.21}$$

and the long range limit reads

$$b(r) \simeq \frac{\phi_0}{2\pi\lambda^2} (\frac{\pi\lambda}{2r})^{1/2} \exp(-\frac{r}{\lambda}) \tag{1.22}$$

The vortex has a normal core with supercurrent flowing around it. The size of the normal core is of the order of ξ, over which the magnitude of the order parameter rises from zero to $|\psi_\infty|$. Fig. 1.3 schematically shows how the order parameter, the coherence length and the magnetic field intensity is behaving in type-I and type-II superconductors.

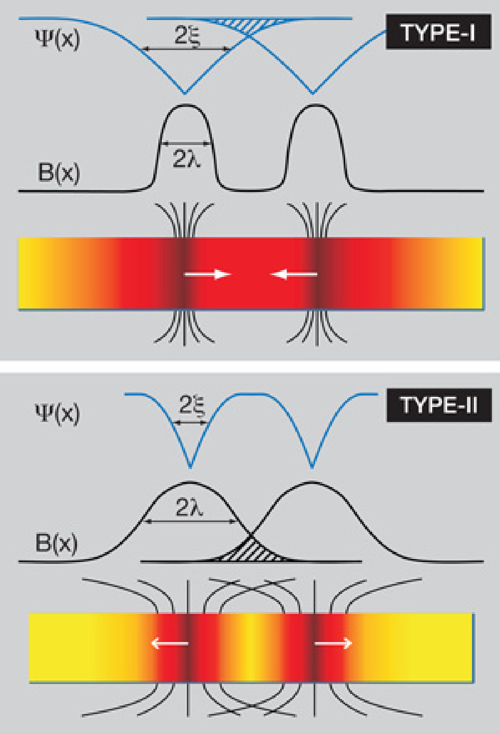

Figure 1.3: The behavior of the magnetic field and the order parameter in type-I and type-II superconductors.

1.5 Flux pinning and the critical state model

Vortices in a type-II superconductor would in the absence of external forces arrange themselves into a hexagonal *flux line lattice* (FLL). In any physical sample, this flux is pinned to defects like voids, grain boundaries, precipitates and dislocations which causes deviations from the hexagonal symmetry. Vortices are affected by currents by the *Lorentz force density*. The Lorentz force density is given by

$$\mathbf{F}_L = \mathbf{j} \times \mathbf{B} \tag{1.23}$$

The force balance on a moving flux line is generally given by

$$\mathbf{F}_L + \mathbf{F}_p + \mathbf{F}_v = 0 \tag{1.24}$$

It is here assumed that the vortices are massless [3]. $\mathbf{F}_p$ is the *pinning force density* and $\mathbf{F}_v$ is the *viscous force density*. Any moving vortex or collection of vortices will induce an electric field

$$\mathbf{E} = \mathbf{B} \times \mathbf{v} \tag{1.25}$$

In the extreme limit where the vortices are pinned so strongly that they hardly move, no viscous forces are at work, and the equation is simplified to

$$\mathbf{F}_L + \mathbf{F}_p = 0 \tag{1.26}$$

Such a situation is denoted as the *critical state* [4]. A current corresponding to the pinning force density can be defined as

$$F_p = j_c B \tag{1.27}$$

The internal current that characterizes this situation is called the *critical current* j_c. In a model by Bean, a field-independent critical current is postulated, while extensions by Kim [5] and others more realistically allows the critical current to be field dependent, $j_c(B)$. The case of a constant j_c is called the *Bean model.* When there is no vortex motion, there is also no dissipation of energy, and any current below j_c can theoretically flow without any resistance. The pinning force on a vortex lattice is not in general equal to the sum of the pinning forces, as the vortex lattice has internal stiffness and will have to be deformed in order to conform to the actual pinning sites. The expression for the magnetic field at depth x from the surface inside a thick superconducting slab in the Bean model can be derived from Ampère's law

$$\frac{dB}{dx} = -\mu_0 j_c \tag{1.28}$$

which is trivial to integrate with $B = B_a$ as boundary condition, obtaining

$$B(x) = B_a - \mu_0 j_c x \tag{1.29}$$

Thus, the magnetic field is falling of linearly inside the sample with slope $\mu_0 j_c$. Such a behavior causes a significant hysteresis, for example if the field is ramped up from zero and then down to zero again, flux will be trapped inside the sample. This state is called the *remnant state.* Fig. 1.4 shows cartoons of the Bean model solutions for the internal magnetic fields B and currents j as the applied magnetic field is ramped up and down. In a thin slab, nonlocal electrodynamics give a different solution [6], [7]

$$B(x) = \frac{\mu_0 j_c d}{\pi} ln \frac{x\sqrt{w^2 - a^2} + w\sqrt{x^2 - a^2}}{a\sqrt{w^2 - x^2}}, a \leq |x| \leq w \tag{1.30}$$

where w is the width of the sample, d is the film thickness and the *penetration depth* is given by

$$a = \frac{w}{cosh(\frac{B_a \pi}{\mu_0 j_c d})} \tag{1.31}$$

This penetration depth can be used to deduce the critical current from a magneto-optical image of a sample on the assumption that the current is approximately field independent. The solution Eq. (1.30) is shown in Fig. 1.5.

Note that no pinned vortex lattice is completely static at temperatures different from the absolute zero, as thermal activation will cause *flux creep.* Also note that this analysis is not applicable for non-static situations. Alternating currents will not flow without resistance even if their magnitude is less than j_c due to viscous forces. In practice, there

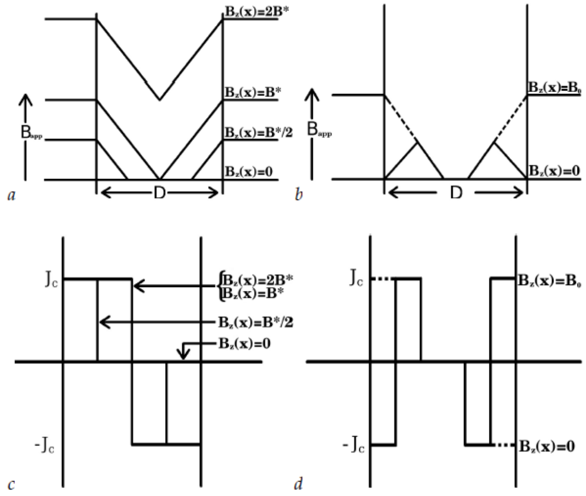

Figure 1.4: Solutions of the Bean model in a slab geometry. a) shows magnetic field distributions inside the sample for applied magnetic fields equal to zero, the field required for full penetration B^* and also for $B^*/2$ and $2B^*$. c) shows the current distributions corresponding to the fields in a). b) shows the internal magnetic field distribution for a ramp up to an applied field $B_0 < B^*$ and a subsequent ramp back to $B = 0$. d) shows the current distributions corresponding to the magnetic history in b).

is also some electrical resistance below j_c. The relation between electric field and current in the superconductor is often parameterized in the form

$$\mathbf{E} = \rho_0 (\frac{j}{j_c})^{n-1} \mathbf{j} \tag{1.32}$$

This is called the *material law* of the superconductor. It reduces to Ohm's law if $n = 1$ and to the Bean model if $n = \infty$. The Bean- and critical state models can also be extended to handle samples with anisotropic j_c. In this case, different currents will flow in the x- and y-directions of the sample. From current conservation inside the sample

$$\nabla \cdot \mathbf{j} = 0 \tag{1.33}$$

this requires that the current turns around at an angle

$$\alpha = \arctan \frac{j_{c,y}}{j_{c,x}} \tag{1.34}$$

$j_{c,x}$ and $j_{c,y}$ are the critical currents in the x- and y-directions, respectively. Fig. 1.6 shows a magneto-optical image of a sample with anisotropic j_c. Notice the dark lines, known as *discontinuity lines* or simply *d-lines*. In the isotropic, flat sample, the d-lines are situated at an angle of 45° from the sample edge. In an anisotropic sample, this is not the case. This angle is generally also magnetic field- and temperature dependent, as the magnitudes

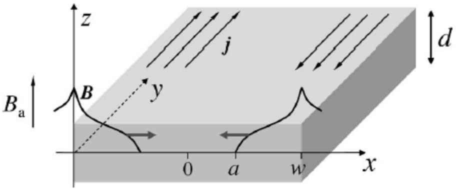

Figure 1.5: Solution of the Bean model in a thin strip geometry.

of the critical currents might have different magnetic field- and temperature dependencies. To be a little more pedantic, there are actually two different kinds of d-lines, both visible in Fig. 1.6. The dark, internal lines where the current **j** changes direction, but $|j|$ is constant is denoted d^+ lines. In contrast, the bright lines at the three visible edges of the sample are denoted d^- lines. d^- lines appear where the magnitude $|j|$ changes [8].

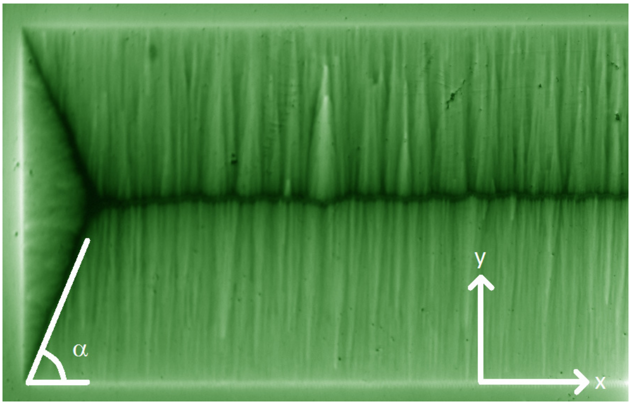

Figure 1.6: A magneto-optical image of a YBCO strip grown on a substrate with tilt angle of 8°. The d^+-line angles relative to the sample edges deviate from 45° and thus indicate anisotropic j_c.

1.6 Thermomagnetic instability

In type-II superconductors, the following feedback loop is present: A moving vortex will dissipate thermal energy at a rate $j \cdot E$. This leads to a local temperature increase, which will increase the probability of other vortices escaping the potential wells they are trapped in, a process called *depinning*. More vortices will then be moved by the Lorentz force, and as Faraday's law states

$$E = -\frac{d\Phi}{dt} \tag{1.35}$$

these vortices will induce an electric field, causing a further thermal energy dissipation and more depinning. In several materials and temperature regimes, this loop has a gain larger than one, one has a thermal runaway, and the material exhibits *thermomagnetic instability.* Often, the resulting avalanche has a dendritic shape, as seen in Fig. 1.7. These *dendrites* are not present at all temperatures and magnetic fields, instead they appear below some temperature and between two threshold fields [9]. It is obviously of practical importance to know where in the parameter space a given superconductor becomes thermomagnetically unstable, as the sudden loss of superconductivity and strong heat dissipation can destroy a device.

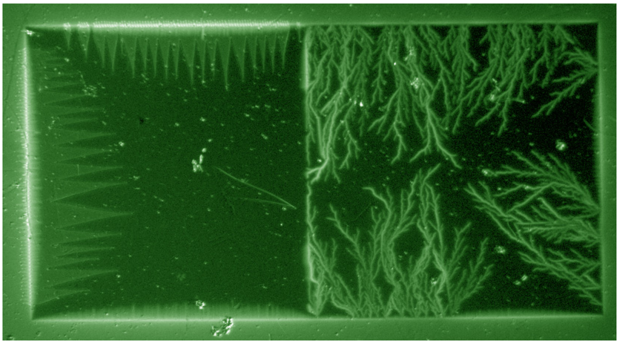

Figure 1.7: NbN sample with the left half covered with a Cu layer. Dendrites are seen in the right half, while they are suppressed by the metal in the left half. Image captured at $T = 4$ K and $B_a = 1.7$ mT.

An instability criterion for a slab of width w can be derived. If the temperature in the sample changes rises from T to $T + \Delta T$ in a short time Δt, one can write that the current density changes to $\Delta j_c = (dj_c/dT)\Delta T$. Such a change will induce an electric field

$$E(x) = \int_{w/2}^{x} \mu_0 \frac{\Delta j_c}{\Delta t} x dx = \frac{\mu_0}{2}(-\frac{\Delta j_c}{\Delta t})(w^2/4 - x^2) \tag{1.36}$$

The energy loss is given by

$$W = \frac{2}{w}\int_0^{\Delta t}\int_0^{w/2} j_c E(x) dx = \frac{\mu_0 j_c w^2}{12}(-\frac{\Delta j_c}{\Delta t})\Delta T \tag{1.37}$$

If the energy dissipation happens fast enough compared to thermal conduction of the material, the temperature rise is given by $\Delta T' = W/C$ where C is the heat capacity.

$$\Delta T' = \frac{\mu_0 j_c w^2}{12C}(-\frac{\Delta j_c}{\Delta t})\Delta T \tag{1.38}$$

If this rise is larger than the initial temperature rise ΔT, the material is thermomagnetically unstable. This can be formulated

$$\frac{\mu_0 j_c w^2}{12C}(-\frac{\Delta j_c}{\Delta t}) > 1 \tag{1.39}$$

The heat dissipation within a dendrite can be so strong that the superconductor goes into the normal state and vortices cease to exist for a short time. Such an avalanche has more complicated physics than a simple rearrangement of the flux lines in the vortex lattice. Films are in general more unstable than bulk samples [6].

1.7 Non-thermal flux avalanches

It was noted by de Gennes in 1966 that the critical state in the Bean model in a thick slab has a similarity with a sandpile [3]. Just as the sandpile arranges itself to have a constant slope equal to the *angle of repose*, the Bean model is characterized by a constant magnetic field gradient and a constant j_c. In thin films, the magnetic field gradient is no longer constant, but j_c is. Some authors consider this to be an evidence of *self-organized criticality* (SOC) [10]. Both systems can through complicated dynamics arrange themselves into a state characterized by a single parameter, which in this context generally also is denoted as a "critical state". The theoretical framework of SOC predicts perturbations of the critical state to result in avalanches distributed by a scale invariant power law both in the spatial and temporal domain. Power laws are however very common in nature, and the more phenomenological concept of *crackling noise* has also been used to describe systems exhibiting power law avalanche statistics [11]. Most simulations in the framework of SOC neglect thermal activation effects and thus focus on non-thermal flux line rearrangements.

Chapter 2

Magneto-optical experiments

In this chapter, a brief description of the experimental method of magneto-optical imaging and the two magneto-optical microscopes used in this work is given.

2.1 Magneto-optical imaging using the Faraday effect

Several techniques can be used to visualize magnetic field distributions. Magneto-optical imaging based upon the *Faraday effect* has several advantages such as locality, extremely good time resolution (picosecond) and good spatial resolution (typically ~ 1 μm). This work utilizes ferrite garnets which, depending on exact chemical composition, can be used at magnetic fields up to B = 70-100 mT. A general review of magneto-optical imaging utilizing the Faraday effect is given in [12].

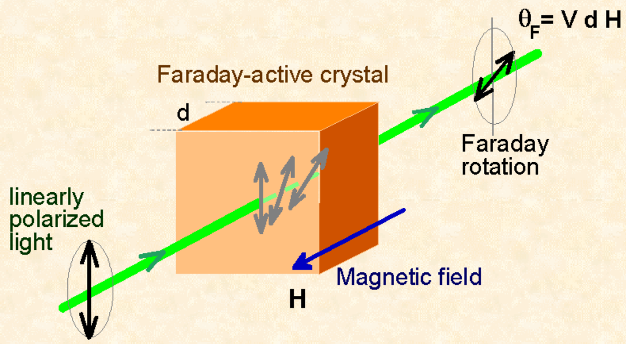

Figure 2.1: Rotation of polarized light in a Faraday active crystal.

The Faraday effect is the rotation of the polarization vector of light in a transparent medium when a magnetic field is applied along the wave vector of the light, as seen in Fig. 2.1. The rotation is proportional to the length of the optical path inside the material.

It is possible to construct an polarization microscope based on this effect. In such a setup, the light beam is first polarized by a polarizer. The beam is then reflected by

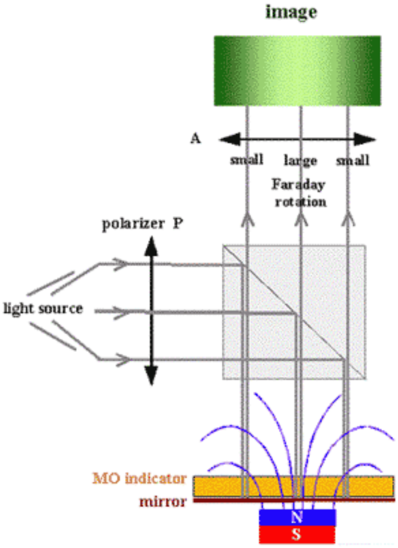

Figure 2.2: Schematic setup of a magneto-optical polarization microscope.

a beam splitter with a partially transparent mirror towards the Faraday active indicator film. The polarization of the light beam then undergoes a Faraday rotation, hits the mirror deposited on the film directly above the magnetic field source and is reflected, undergoing an equivalent Faraday rotation in the same direction as the first and is transmitted back though the beam splitter. To generate the image, the light is at last transmitted through an analyzer. If the angle between the polarizer and the analyzer is 90°, dark areas in the image will correspond to no Faraday rotation and thus no magnetic field, while brighter areas correspond to Faraday rotation due to magnetic field in the area. However, as will become obvious in the chapter about quantitative magneto-optics, this configuration has the lowest sensitivity. For higher sensitivity one can instead operate the setup at a relative angle between polarizer and analyzer of 45°. A sketch of a magneto-optical microscope can be seen in Fig. 2.2

The indicator film is made of three layers: An aluminium mirror, a ferrite garnet Faraday rotating layer and a gadolinium gallium garnet (GGG) substrate. A sketch is shown in Fig. 2.3. These substrates are not regularly produced anymore and are starting to be hard to come by.

2.2 Experimental setups

Two magneto-optical systems have been used in this work. The first setup consists of an Oxford helium flow cryostat with magnet coils around it, a Leica polarizing microscope, an Oxford ITC503 temperature controller, a Delta Elektronika SM 7020-D power supply,

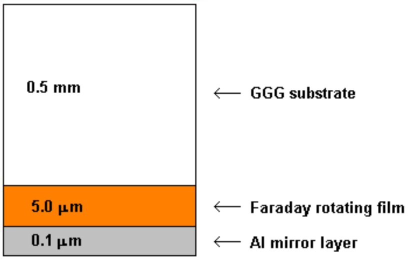

Figure 2.3: Schematic of an indicator film with three layers.

a RetigaExi 12-bit CCD camera, a liquid helium Dewar tank with a helium transfer tube and, of course, a computer. Light is supplied by a mercury lamp. A Pfeiffer vacuum pump is used to evacuate the cryostat down to $O(10^{-5})$ mbar before it is cooled. The helium transfer tube must also be evacuated down to $O(10^{-5})$ mbar. Evacuation and cooling down takes about 30 minutes. This setup can reach about T = 3.5 K and the maximum magnetic field from the coils is B = 85 mT. It can study most phenomena of interest in magneto-optical imaging of superconductors including dendrites and some type-I materials with a high T_c like Pb. It is however expensive to run due to its consumption of helium, which is not recovered. A picture of the microscope with the flow cryostat is shown in Fig. 2.4.

The second setup is a DE-204 SF closed-cycle cryostat from ARS combined with an Olympus microscope. It utilizes an ARS-4HW compressor and an ARS Coolpac water cooler, though the compressor can also be cooled with tap water. The cold finger is thermally connected to the cooling element in the cryostat through a layer of helium exchange gas, ensuring a good vibration insulation. This gas is supplied from an external bottle and its pressure is regulated to be below 1.5 bar by an automatic release valve. The exchange gas volume has another manual valve which is opened and closed 20-30 times before cooling down to allow the helium to replace any air inside. If this is not done properly, the air will freeze, causing strong vibrations to be transferred from the cooling element to the cold finger. A Scientific Instruments Model 9700 temperature controller monitors the temperature. The minimum achieved temperature of the setup is about T = 8.5 K, which takes about 3 hours of cooling to achieve. The maximum magnetic field supplied by its magnet coils is B = 75 mT. The same camera and computer is used in this setup, together with a similar vacuum pump and power supply. This setup should also be evacuated down to $O(10^{-5})$ mbar. Due to the higher minimum temperature of this setup, it cannot study type-I superconductors or dendrites efficiently. It is however good for general experiments regarding current distributions, defect structure and penetration depths at higher temperatures. Also, it is inexpensive to run as it consumes very little helium. This setup is shown in Fig. 2.5.

Figure 2.4: The setup with the helium flow cryostat.

2.3 Practical magneto-optical experiments at low temperatures

Before mounting, samples and indicator films should be inspected under an ordinary microscope with a few times magnification. One will then easily see dust, grease or other kinds of dirt. If the sample is dirty, it should be cleaned in toluene and wiped clean with soft, lint-free wipes. It is very important to note that even small scratches on a sample often render them useless, as the flux distribution inside the sample below T_c can be severely disturbed. It is also easy to damage the mirror deposited on indicator films. Samples should also be kept in an exicator with silica gel to absorb moisture to avoid degradation and oxidation. One can additionally evacuate the exicator for air to further reduce the chance of degradation, the only exception is maybe perovskite HTS materials like YBCO, where the oxygen stoichiometry can be disturbed by outgassing into the vacuum.

Samples are mounted on a cold finger. Vacuum grease will fix the sample physically and ensure a good thermal contact between the cold finger and the sample. The magneto-optical indicator film is placed directly on top of the sample, and it is important that it is not tilted relative to it, as partial blurring of the image will result. It must also be restrained to not slip away from the sample as a result of vibrations. 4 L-shaped pieces of aluminum tape will ensure this, as shown in Fig. 2.6. A radiation shield of aluminum

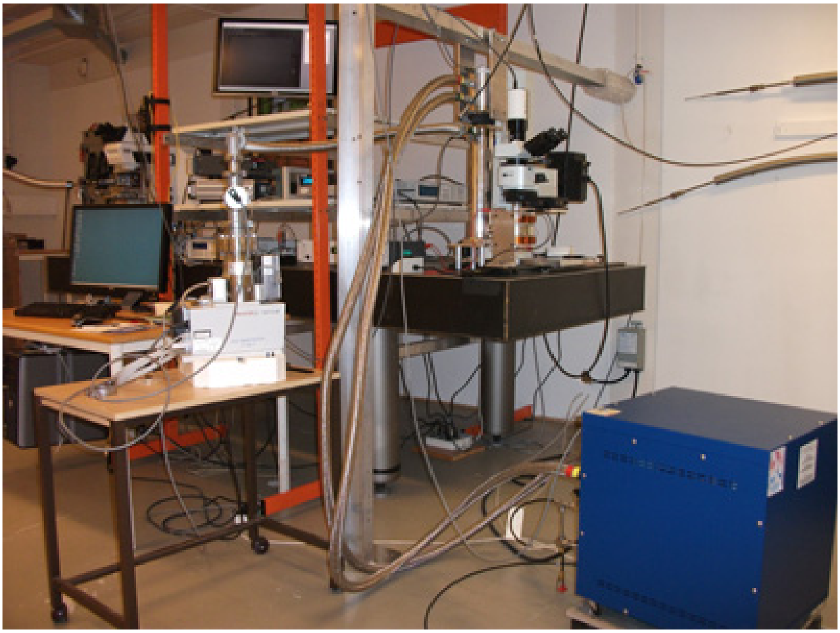

Figure 2.5: The setup with the closed-cycle cryostat.

is attached around the cold finger before it is placed in the cryostat. This shield and all other metal surfaces should be free of fingerprints and grease, as these are opaque and radiate in the infrared range.

It is very important to avoid getting vacuum grease between the indicator film and the sample. At low temperatures, the vacuum grease will solidify and stress the indicator film. This causes ”stripe domains” to appear and ruins the image. Also, the grease should be evenly distributed below the sample. If there is air trapped below the sample, sudden displacements can result from thermal volume changes.

Different kinds of vacuum grease exist. Our lab has used Dow Corning, Apiezone and Cryocon grease from ARS. The first is fairly standard and works OK in most circumstances. Apiezone has better thermal conductivity, but is harder to distribute evenly as it is more sticky. The Cryocon grease is maybe the best, it contains tiny copper particles to ensure an even better thermal conductivity. In the closed-cycle cryostat, this is important, as its cooling power is much smaller than the cooling power of the flow cryostat.

Both setups are able to deliver very good images with 20x magnification. 50x is attainable, but these images are dark and suffer from depolarization effects. The higher the magnification, the worse are vibration effects and vibration insulation becomes more and more important. Even a person walking in the lab will disturb the image at 20x. For the closed cycle cryostat, the vibration insulation is very good and the small vibrations seen are mostly coming from the vacuum pump. The flow cryostat is somewhat more

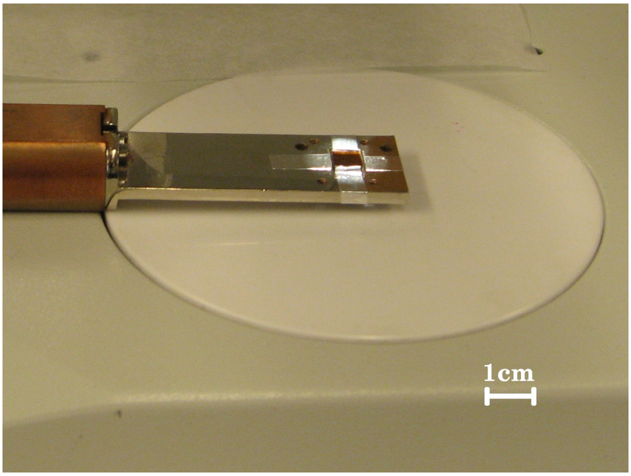

Figure 2.6: Cold finger, magneto-optical indicator film and aluminum L-shapes. A NbN sample is mounted below the indicator. Figure from [13].

plagued from vibrations, they are coming from both the vacuum pump and the helium pump.

To transfer helium gas from a Dewar tank to a flow cryostat, a transfer tube is used. It must be slowly inserted into the Dewar tank to let the helium replace the air inside (obviously the valve on top of the transfer tube must be open). Otherwise a blockage of frozen air will result. If this happens either during insertion or running the experiment, the tube must be taken out and dried, preferably with a heat gun. One must also run air through it to dry up any moisture inside of it.

The flow cryostat should not be cooled faster than 10°C per minute, as excessive thermal stress can degrade the materials in setup in the long run. Such concerns are minimal for the closed-cycle cryostat, as it is not able to cool nearly that fast. When heating up again, air must not be allowed to enter the vacuum inside the setups before the temperature has reached room temperature. Otherwise, condensation inside the setup will result, possible causing degradation.

Magnet coils are air-cooled and must not be allowed to overheat. A rule of thumb is that they should not become hotter than what is comfortable to touch (50°C). This is a general problem for any experiment using a high field for extended periods of time. Water cooling could be implemented, but would make the setup more bulky and impractical.

Light sources should be switched on and off as little as possible, as this shortens their lifespan. The current light sources are AC powered arc lamps running of the mains. This induces a spurious flickering in the images. Although this effect is only about a few percent (in the case of the flow cryostat setup), it would be an improvement to use dc powered green high-intensity LEDs. A green laser can also be used, but will require more safety precautions and introduce interference noise.

Chapter 3

Quantitative magneto-optics

Qualitative magneto-optical imaging can locally and in real-time reveal features of the flux penetration pattern, like penetration depths, defects, anisotropic penetration and also dynamic features like flux creep, flux avalanches and dendrites. However, for obtaining information about magnetic field values and current densities, a quantitative treatment is required. This is a much more complicated task that first involves calibrating the measured light intensity from the indicator as a function of local magnetic field. Afterwards, the current pattern can be deduced with inversion of the Biot-Savart law. In order to get further with this problem, the physics of indicator films and the calibration of magneto-optical images will first have to be discussed.

3.1 Ferrite garnets with in-plane magnetization

Several types of indicator films have been used for magneto-optical imaging: Europium selenide (EuSe), ferrite garnets with out-of-plane magnetization and ferrite garnets with in-plane magnetization. In this work, the focus is on the latter, which in use shows a characteristic and, sometimes, problematic sawtooth-pattern of magnetic domains. Their advantages include a high and rather constant Faraday rotation in a temperature range covering the lowest attainable temperatures in a He-4 cryostat and above the T_c of HTS materials. The spontaneous in-plane field B_A of these garnets are in the range 70-100 mT, if a larger field is applied, the rotation saturates. Unfortunately, the in-plane magnetized garnets are also sensitive to the in-plane field components B_x and B_y, which will cause a non-locally reduced Faraday rotation and thus underestimation of the local B_z [14]. To discuss this problem, we first define a coordinate system where the magneto-optical indicator film is lying in the horizontal plane, see Fig. 3.1.

The interaction energy of the indicator film with the magnetic field B is the sum of the anisotropy energy and the magnetostatic energy

$$E_{int} = E_A \sin^2\phi - \mathbf{B} \cdot \mathbf{M}_s \tag{3.1}$$

which can be expanded as

$$E_{int} = E_A \sin^2\phi - B_{\|} M_s \cos\phi - B_{\perp} M_s \sin\phi \tag{3.2}$$

where M_s is the spontaneous magnetization vector, related to the anisotropy energy and spontaneous in-plane field as $2E_A \equiv B_A M_s$. As seen in Fig. 3.1, there is symmetry

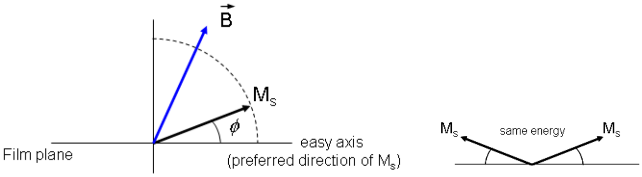

Figure 3.1: Left: Coordinate system. Right: Symmetry of the interaction energy in an external field.

around the vertical axis and configurations where the angle ϕ between the magnetization vector and the horizontal plane are identical have the same energy. In order to find the equilibrium angle of the spontaneous magnetization, the expression is differentiated with respect to ϕ and set equal to 0. The case $B_{\parallel} = 0$, $B_{\perp} = B$ is simple to treat analytically

$$0 = (2E_A \sin\phi - BM_s)\cos\phi \tag{3.3}$$

Eq. (3.3) has the nontrivial solution

$$\sin\phi = \frac{BM_s}{2E_A} = \frac{B}{B_A} \tag{3.4}$$

The Faraday rotation is generally given by

$$\theta_F = VtM_s \sin\phi = \theta_{sat}\frac{B}{B_A} \tag{3.5}$$

where V is the Verdet constant of the film, t is the thickness and the product $VtM_s \equiv \theta_{sat}$. The rotation is clearly proportional to the applied field inside a range defined by $\pm B_A$, outside of which the rotation saturates to θ_{sat}. The rotation as a function of the magnetic field is plotted in Fig. 3.2.

Malus' law for crossed polarizer-analyzer can be written

$$I = I_0 \sin^2(\theta_F) + I_{leak} \tag{3.6}$$

Combining Eqs. (3.5) and (3.6) gives the light intensity as a function of applied field

$$I = I_0 \sin^2(\theta_{sat}\frac{B}{B_A}) + I_{leak} \tag{3.7}$$

which can be solved for

$$B = \frac{B_A}{\theta_{sat}} \arcsin\sqrt{\frac{I - I_{leak}}{I_0}} \tag{3.8}$$

This approximation is applicable for $B_{\parallel} \ll B_A$. A more general expression for the light intensity in case of relative polarizer-analyzer angles of θ is

$$I = I_0 \sin^2(\theta_{sat}\frac{B}{B_A} + \theta) + I_{leak} \tag{3.9}$$

giving a corresponding equation for the magnetic field

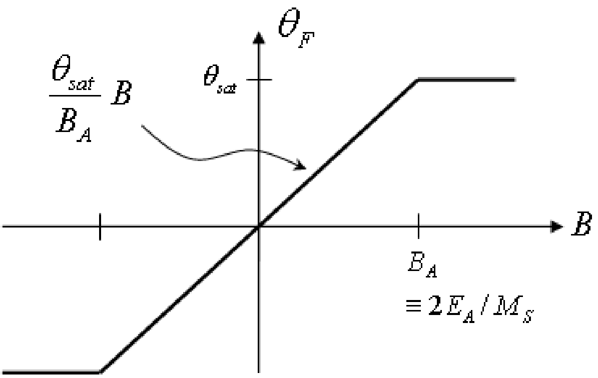

Figure 3.2: Faraday rotation in the indicator film for $B = B_\perp$ and $B_\parallel = 0$.

$$B = \frac{B_A}{\theta_{sat}}(\arcsin\sqrt{\frac{I - I_{leak}}{I_0}} - \theta) \tag{3.10}$$

The most general case with a significant $B_\parallel$ is in theory also analytically solvable, but requires the extremely complicated solution of a quartic equation. With an EuSe indicator film, one would get a similar functional dependency, but in this case the Faraday rotation angle is just the product of the Verdet constant and the thickness, so the coefficient in front of the parenthesis in Eq. (3.10) would instead be $1/Vt$.

3.2 Calibration

As the light source does not have an isotropic beam and the intensity of the Faraday rotated light is not a linear function of the local field, the image data must be calibrated if the local values of the magnetic fields and the currents are to be deduced. The large temperature range of the ferrite garnets allows the response of the indicator film as a function of magnetic field to be recorded above the T_c of the superconductor. A series of images of the light intensity for each pixel $I(x, y)$ can be obtained where the local field in the indicator film is just the applied magnetic field $B_a(x, y)$. Images can then be captured below T_c and from the known, monotonic relationship between B and I, $B_z(x, y)$ can be reconstructed. It is here assumed that the light response is approximately independent of the temperature at temperatures at and below the T_c of the material in question. The intensity for crossed polarizers is an s-shaped function of B_a, which can be approximated at small B_a as a second order polynomial in B_a. In general, the best possible fit function depends on the ratio of the saturation field of the indicator relative to the maximum applied field. A typical behavior of the light response as a function of B_a is shown in Fig. 3.3.

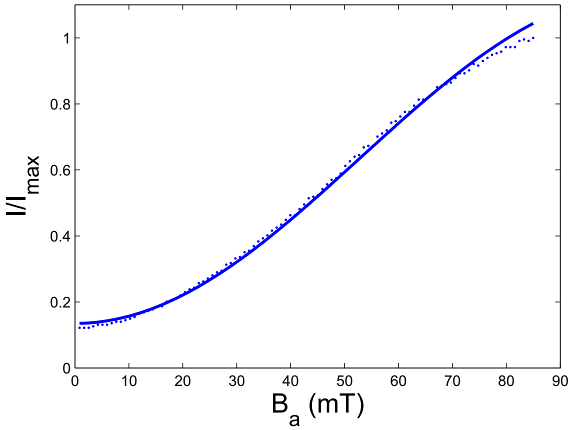

Figure 3.3: Typical relationship between intensity and magnetic field for a pixel. A fit to Eq. (3.7) is shown with $I_{leak}/I_0 = 0.135$ and $\theta_{sat}/B_A = 0.0149$. θ was set to zero, a slightly better fit can be obtained by making it a fit parameter.

3.3 Biot-Savart law in Fourier space

The Biot-Savart law reads in full generality

$$\mathbf{B}(\mathbf{r}) = \frac{\mu_0}{4\pi} \int \frac{\mathbf{j}(\mathbf{r'}) \times (\mathbf{r} - \mathbf{r'})}{|\mathbf{r} - \mathbf{r'}|} d^3r' \qquad (3.11)$$

The three components of the magnetic flux density generated by a three-dimensional current distribution can thus be written

$$B_x(x,y,z) = \frac{\mu_0}{4\pi} \int\int\int \frac{j_y(x',y',z')(z-z') - j_z(x',y',z')(y-y')}{\sqrt{[(x-x')^2 + (y-y')^2 + (z-z')^2]^3}} dx'dy'dz' \qquad (3.12)$$

$$B_y(x,y,z) = \frac{\mu_0}{4\pi} \int\int\int \frac{j_z(x',y',z')(x-x') - j_x(x',y',z')(z-z')}{\sqrt{[(x-x')^2 + (y-y')^2 + (z-z')^2]^3}} dx'dy'dz' \qquad (3.13)$$

$$B_z(x,y,z) = \frac{\mu_0}{4\pi} \int\int\int \frac{j_x(x',y',z')(y-y') - j_y(x',y',z')(x-x')}{\sqrt{[(x-x')^2 + (y-y')^2 + (z-z')^2]^3}} dx'dy'dz' \qquad (3.14)$$

The "forward" calculation of the magnetic field from a three-dimensional current distribution is always possible. An example is shown below: In a series of MgB$_2$ samples with half of the rim covered with a gold layer, the magneto-optical images suggest a different $j_{c,1}$ in the gold covered area as opposed to the $j_{c,2}$ in the sample outside is. A representative example of this behavior is shown in Fig. 3.4.

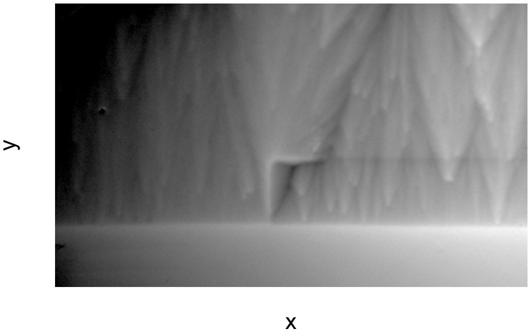

Figure 3.4: MgB_2 sample with gold coating, T = 3.5 K and B_a = 65.1 mT. The gold coated area has a rectangular shape and is situated in the lower right half of the sample.

Current conservation limits possible flow patterns to a single one shown in Fig. 3.5 and the resulting field distribution and magneto-optical image from a ratio $j_{c,1}/j_{c,2}$ was calculated. It is seen that the calculated image has the same d-lines as the original image, showing that this current flow pattern is indeed consistent with the observed image.

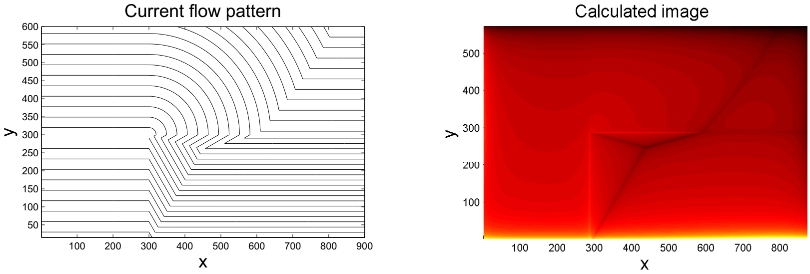
Current flow pattern

Calculated image

Figure 3.5: Left: Current lines compatible with the magneto-optical image in Fig. 3.4. Right: Calculated magneto-optical image from the currents in the left image.

In contrast, the inverse problem does not in general have a unique solution. For a sample with $d < 2\lambda$, it is a good approximation to consider the current density to be constant over the z-direction. For thicker samples, one can determine an average of the current over the thickness. It is also assumed in the following that j_z is zero. These assumptions result in the following equations for the magnetic field components in a height h above a thin sample with thickness d

$$B_x(x, y, h) = \frac{\mu_0}{4\pi} \int_{-d/2}^{d/2} \int \int \frac{j_y(x', y')h}{\sqrt{[(x - x')^2 + (y - y')^2 + h^2]^3}} dx'dy'dz' \tag{3.15}$$

$$B_y(x, y, h) = \frac{\mu_0}{4\pi} \int_{-d/2}^{d/2} \int \int \frac{-j_x(x', y')h}{\sqrt{[(x - x')^2 + (y - y')^2 + h^2]^3}} dx'dy'dz' \tag{3.16}$$

$$B_z(x, y, h) = \frac{\mu_0}{4\pi} \int_{-d/2}^{d/2} \int \int \frac{j_x(x', y')(y - y') - j_y(x', y')(x - x')}{\sqrt{[(x - x')^2 + (y - y')^2 + h^2]^3}} dx'dy'dz' \tag{3.17}$$

As shown by Roth [15], it is possible to calculate a two-dimensional current distribution from the a two-dimensional image of B_z measured in a fixed distance from the film. Roth utilized the fact that the Biot-Savart law has translational symmetry and that the convolution theorem therefore can be applied. This method was first applied to magneto-optical imaging by Jooss [16]. The Green's function

$$g(x - x', y - y', h) = \frac{\mu_0}{4\pi} \frac{h}{[(x - x')^2, (y - y')^2, h)]^{3/2}} \tag{3.18}$$

has an analytical Fourier transform

$$\widetilde{g}(k_x, k_y, h) = \frac{\mu_0}{2} e^{-h\sqrt{k_x^2 + k_y^2}} \tag{3.19}$$

Using this transform, the two-dimensional Fourier transforms of Eq. (3.15), Eq. (3.16) and Eq. (3.17) can be written

$$\widetilde{B}_x(k_x, k_y, h) = \frac{\mu_0 d}{2} \widetilde{j}_y(k_x, k_y) e^{-hk} \tag{3.20}$$

$$\widetilde{B}_y(k_x, k_y, h) = -\frac{\mu_0 d}{2} \widetilde{j}_x(k_x, k_y) e^{-hk} \tag{3.21}$$

$$\widetilde{B}_z(k_x, k_y, h) = i\frac{\mu_0 d}{2} (\frac{k_y}{k} \widetilde{j}_x(k_x, k_y) - \frac{k_x}{k} \widetilde{j}_y(k_x, k_y)) e^{-hk} \tag{3.22}$$

where $k = \sqrt{k_x^2 + k_y^2}$ and the integration over dz' has been carried out through a simple multiplication with the film thickness d. The equation Eq. (3.22) are simplified when considering the magnetization scalar field g($\mathbf{r}$), which relates to the current as

$$\mathbf{j(r)} = \nabla \times \hat{z}g \tag{3.23}$$

As the divergence of the curl of a scalar field always is zero, this form ensures that the sheet current density has no divergence, which again is required by current conservation inside a superconductor with no external current sources

$$\nabla \cdot \mathbf{j(r)} = \nabla \cdot (\nabla \times \hat{z}g) = 0 \tag{3.24}$$

In components this can be written $j_x(x, y) = \partial g(x, y)/\partial y$ and $j_y(x, y) = -\partial g(x, y)/\partial x$. In Fourier space, the partial derivatives are performed by multiplying $\widetilde{g}(k)$ by $-ik_y$ and $-ik_x$, respectively. This enables us to rewrite Eq. (3.22) as

$$\widetilde{B}_z(\mathbf{k},z) = \frac{\mu_0 d}{2}(\frac{k_y^2}{k}\tilde{g}(\mathbf{k}) + \frac{k_x^2}{k}\tilde{g}(\mathbf{k}))e^{-hk} \tag{3.25}$$

which can be simplified to

$$\widetilde{B}_z(\mathbf{k},z) = \frac{\mu_0}{2}dk\tilde{g}(\mathbf{k})e^{-hk} \tag{3.26}$$

Thus, the magnetic field can then be calculated from the magnetization, and this is especially simple in Fourier space, where one can see that the Biot-Savart law for B_z is a local function of g. For the Bean model, the magnetization functions are straight planes with slope j_c. One should also note the product of the height above the sample and the wave number in the exponential in Eq. (3.26). This tells us that the B_z is a low pass filtered g. Proximity of the indicator film to the current sheet is thus important to avoid blurring of the image of B_z. If one wants to go the other way, i.e. obtain the currents from a measurement of B_z, one solves Eq. (3.26) for $\tilde{g}(\mathbf{k})$

$$\tilde{g}(\mathbf{k}) = \frac{2}{\mu_0 dk}\widetilde{B}_z(\mathbf{k},z)e^{hk} \tag{3.27}$$

and then the currents are found from $j_x(x,y) = \partial g(x,y)/\partial y$ and $j_y(x,y) = -\partial g(x,y)/\partial x$ The absolute value of the current density is then found by $|j| = \sqrt{j_x^2 + j_y^2}$. This *inversion* can be done for experimentally obtained magneto-optical images after they have been calibrated into two-dimensional maps of $B_z(x,y)$.

3.4 Fast Fourier transformation

In order to implement the calculations numerically, a quick detour to Fourier transformations is needed. The Fourier transformation and its inverse are defined by

$$\widetilde{f}(k) = \int_{-\infty}^{\infty} dx f(x)e^{-ikx} \tag{3.28}$$

$$f(x) = \frac{1}{2\pi}\int_{-\infty}^{\infty} dk\widetilde{f}(k)e^{ikx} \tag{3.29}$$

The *Discrete Fourier Transform* (DFT) is the numerical discretization of the Fourier transform and its inverse. On a grid of size L with N points, they are defined by

$$\widetilde{g}_n = \sum_{j=0}^{N-1} g_j e^{-i\frac{2\pi jn}{N}} \tag{3.30}$$

$$g_n = \frac{1}{N}\sum_{n=0}^{N-1} \widetilde{g}_n e^{i\frac{2\pi jn}{N}} \tag{3.31}$$

where the continuous integration variables are replaced with discrete counterparts: $x \longrightarrow x_n = \frac{Ln}{N}$ and $k \longrightarrow k_j = \frac{2\pi j}{L}$. As a consequence of the Nyquist-Shannon theorem, the Brillouin zones will have to be rearranged to yield correct results, so in practice

$$k_j = \frac{2\pi}{L}(j - \frac{N}{2}) \tag{3.32}$$

The convolution theorem states that the Fourier transform of a convolution of functions is the product of Fourier transforms point by point

$$\int_{-\infty}^{\infty} dx' f(x')g(x-x') = \frac{1}{2\pi}\int_{-\infty}^{\infty} dk\widetilde{f}(k)\widetilde{g}(k)e^{ikx} \tag{3.33}$$

which in a discrete form reads

$$\sum_{l=0}^{N-1} g_l h_{n-l} = \frac{1}{N}\sum_{n=0}^{N-1} \widetilde{g}_n \widetilde{h}_n e^{i\frac{2\pi jn}{N}} \tag{3.34}$$

A DFT requires $O(N^2)$ operations for each dimension. The *Fast Fourier Transform* (FFT) is any fast algorithm to compute the DFT of a function. The two dimensional FFT requires $N_xN_y(1+2log(N_xN_y))$ operations where N_x and N_y are the dimensions of the grid. This is obviously a huge improvement over the DFT, which would require $O((N_xN_y)^2)$ operations for a two dimensional grid.

A DFT is periodic, and if one tries to sample a function that is not periodic, this will introduce an error. As a consequence, one should ensure periodic boundary conditions when sampling magneto-optical images by for example including the indicator film around it. The finite size of an image also introduces artifacts in the form of a superlattice of spurious current distributions. The imaged area should be at least a factor 2 larger than the sample to reduce this effect.

It is also possible to invert the Biot-Savart law with matrix inversion. This approach requires $O((N_xN_y)^3)$ operations. The Toeplitz symmetry of the integral kernel of the Biot-Savart law has been utilized by Wijngaarden et al. to reduce the number the number of operations to $O((N_xN_y)^{2.25})$.

3.5 Magnetic field to current inversion

Having discussed the physics of in-plane magnetized ferrite garnet indicator films, calibration and the mathematics of FFTs, it is now possible to proceed to inversion of the Biot-Savart law. It should theoretically be simple to extract current distributions from the calibrated magneto-optical images by applying the inverse Biot-Savart in Fourier space and calculating the magnetization g and differentiating it to get j_x and j_y.

In practice, there are several problems. Defects in the superconducting film and in the magneto-optical indicator perturbs the field and the resulting current pattern is sensitive to small distortions in the magnetic field. Even worse are sawtooth-shaped magnetic domains in the indicator film. As mentioned, the indicator film is also sensitive to the in-plane component $B_{xy} = \sqrt{(B_x \cdot \mathbf{i})^2 + (B_y \cdot \mathbf{j})^2}$, which non-locally reduces Faraday rotation and causes an underestimation of B_z. This problem is most pronounced for strong induced currents resulting from a high B_a. It manifests itself as an unphysical current outside the sample and sharp, unphysical peaks in the current density close to the sample edge. At low B_a, a "naïve" inversion, disregarding the in-plane component, will give a good approximation to the actual current distribution. Sawtooth-shaped domains can be removed, or, at least, moved by applying a small in-plane field. In Fig. 3.6, maps of magnetic field values B_z obtained by calibration of raw images and the corresponding inverted current densities $|j|$ are shown for a d = 200 nm thick YBCO film grown on a 14° tilted substrate.

Cross sections of the B_z maps and the $|j|$ maps in Fig. 3.6 are shown in Fig. 3.7. Both an unperturbed cross section and a cross section perturbed by a domain is shown. At such

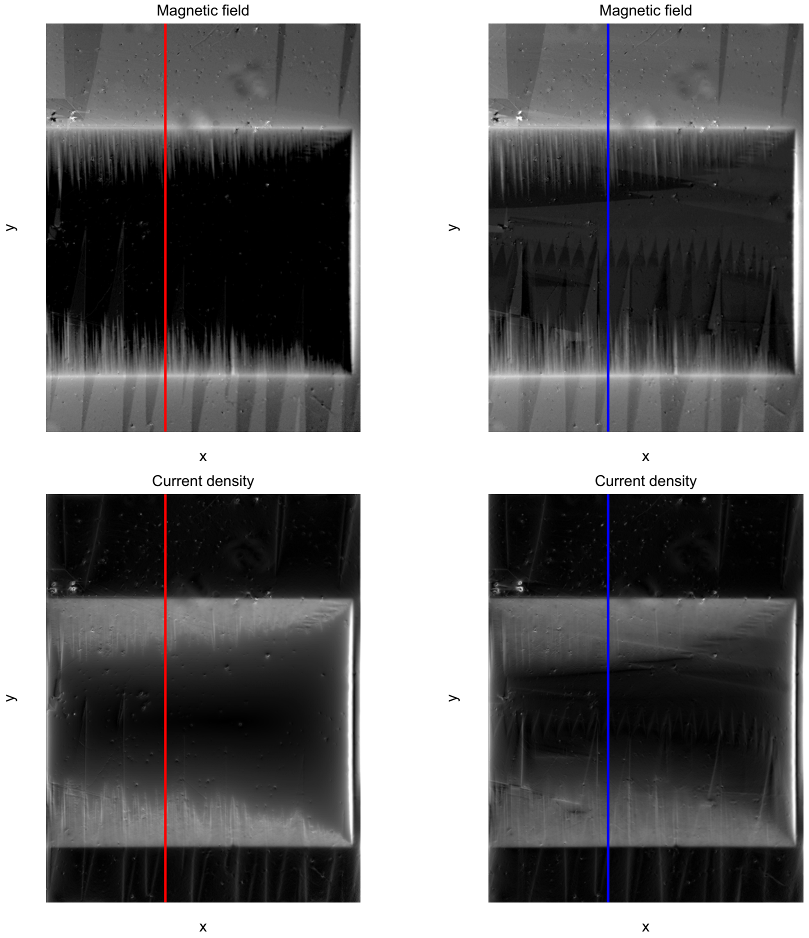

Figure 3.6: Magnetic field maps and current density maps. Left: Maps not significantly perturbed by domains. Right: Maps significantly perturbed by domains. The measurements are obtained with $B_a = 8.5$ mT and $T = 4$ K on a YBCO film on a 14° tilted substrate.

a small applied field, the in-plane corrections is small and the ”naïve” inversion scheme reproduces a Bean-model like current profile which can be seen in Fig. 3.8

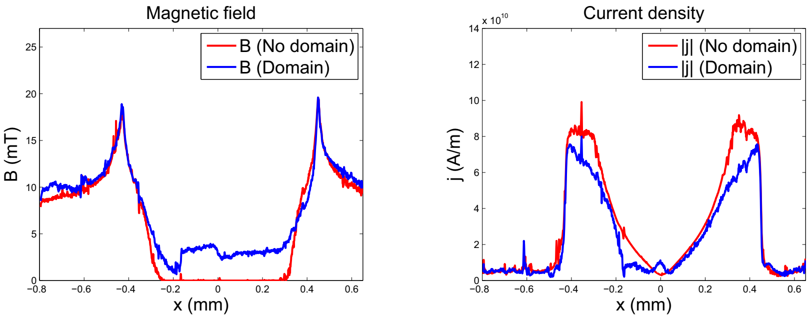

Figure 3.7: Cross-sections of magnetic field maps and current density maps. The measurements are obtained with $B_a = 8.5$ mT and $T = 4$ K on a YBCO film on a 14° tilted substrate.

$$j_x = \begin{cases} -j_c & , -a < x \leq -x_p \\ \frac{2j_c}{\pi} tan^{-1}(\frac{x}{a}\sqrt{(a^2 - x_p^2)/(x_p^2 - x^2)}) & , -x_p < x < x_p \\ j_c & , x_p \leq x < a \end{cases} \tag{3.35}$$

This is somewhat surprising given the intricate filamentary structure of the YBCO sample. It is also seen in figures Fig. 3.7 and Fig. 3.8 that the B_z maps and $|j|$ maps are severely perturbed by domain patterns in the indicator film. Experiments have shown that it is possible to improve the ”naïve” inversion to higher magnetic fields by use of an iterative algorithm [17].

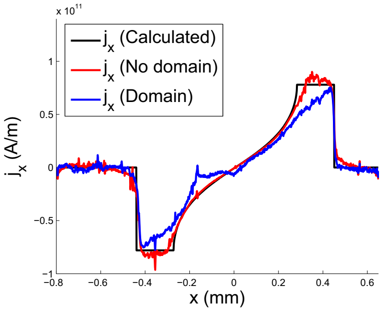

Figure 3.8: Perturbed and unperturbed current densities together with a fit to the Bean model. $j_c = 0.78 \cdot 10^{11}$ A/m^2, $a = 0.44$ mm and $x_p = 0.28$ mm

Bibliography

[1] T. Matsushita, Flux pinning in superconductors, Springer, 2010.

[2] A. A. Abrikosov, On the magnetic properties of superconductors of the second group, Sov. Phys. JETP **5** (1957) 1174.

[3] T. H. Johansen, E. Altshuler, Experiments in vortex avalanches, Rev. Mod. Phys. **76** (2004) 471.

[4] C. P. Bean, Magnetization of hard superconductors, Phys. Rev. Lett. **8** (1962) 250.

[5] Y. B. Kim, C. F. Hempstead, A. R. Strnad, Magnetization and critical supercurrents, Phys. Rev. Lett. **129** (1963) 528.

[6] D. V. Shantsev, A. V. Bobyl, Y. M. Galperin, T. H. Johansen, S. I. Lee, Size of flux jumps in superconducting films, Phys. Rev. B **72** (2005) 24541.

[7] E. H. Brandt, M. Indenbom, Type-ii superconductor strip with current in a perpendicular magnetic field, Phys. Rev. B. **48** (1993) 1289312906.

[8] T. H. Schuster, H. Kuhn, M. V. Indenbom, Discontinuity lines in rectangular superconductors with intrinsic and extrinsic anisotropies, Phys. Rev. B. **52** (1995) 1562115626.

[9] V. V. Yurchenko, D. V. Shantsev, T. H. Johansen, M. R. Nevala, I. J. Maasilta, K. Senapati, R. C. Budhani, Reentrant stability of superconducting films and the vanishing of dendritic flux instability, Phys. Rev. B. **76** (2007) 092504.

[10] P. Bak, C. Tang, K. Wiesenfeld, Self-organized criticality: An explanation of 1 / f noise, Phys. Rev. Lett. **59** (1987) 381–387.

[11] J. P. Sethna, Crackling noise, Nature **410** (2001) 242.

[12] C. Jooss, J. Albrecht, H. Kuhn, S. Leonhardt, H. Kronmuller, Magneto-optical studies of current distibutions in high-T_c superconductors, Rep. Prog. Phys. **65** (2002) 651.

[13] K. Eliassen, Master thesis, UiO, 2008.

[14] T. H. Johansen, M. Baziljevich, H. Bratsberg, Y. Galperin, P. E. Lindelof, Y. Shen, P. Vase, Direct observation of the current distribution in thin superconducting strips using magneto-optical imaging, Phys. Rev. B. **54** (1996) 16264.

[15] B. J. Roth, N. G. Sepulveda, J. P. Wikswo, Jr., Using a magnetometer to image a two-dimensional current distribution, J. Appl. Phys. **65** (1989) 361.

[16] C. Jooss, R. Wartmann, A. Forkl, H. Kronmüller, High-resolution magneto-optical imaging of critical currents in $YBa_2Cu_3O_{7-\delta}$ thin films, Physica C **299** (1998) 215.

[17] F. Laviano, D. Botta, A. Chiodoni, R. Gerbaldo, G. Ghigo, L. Gozzelino, S. Zanella, E. Mezzetti, An improved method for quantitative magneto-optical analysis of superconductors, Supercond. Sci. Technol. **16** (2003) 71.

Part II

Papers

Summary

This work includes six articles, of which I am the first author of three and a co-author of three. The research includes both fundamental physics of superconductors including statistical, nonlinear phenomena and physics relevant to applications such as measurements of critical currents and sample quality.

Paper 1 is a study of the phase diagram of thermomagnetic instability in NbN. Previous research activities have shown and explained the existence of upper and lower threshold fields for the thermomagnetic instability seen in many superconductors. However, what has not been investigated is why the threshold fields are different when the field is rising compared to when it is falling. It is obvious that there is a large hysteresis in the critical state model, for example, at zero applied field after a cycle of magnetization, there can be a strong magnetic field inside the superconductor from trapped flux. Dendrites are seen to nucleate from the edges and it was then assumed that the different applied fields at which dendrites appears should correspond to more or less identical local fields close to the edges of the sample.

In the paper, it is shown that the local field- and current values at the edges are indeed of similar values, thus confirming the prediction. A phase diagram of presence of the instability was measured, showing the effects of magnetic hysteresis. In this work, I did experiments and performed data analysis.

Paper 2, 3 and 4 deals with smooth and intermittent flux dynamics in YBCO samples grown on tilted, ”staircase looking” substrates. The growth on such substrates improves the alignment of YBCO grains and was originally intended to improve the critical current of YBCO wires. In addition, anti-phase boundaries are introduced, which act as pinning centers and further increase the critical current. They are also used for the production of Josephson junctions.

It turns out that flux penetration in such samples is also interesting from a more fundamental point of view. Such samples contain extended defects which form quasi-one-dimensional channels for flux penetration. They have been studied before by other groups, but to our knowledge, nobody has reported intermittent flux penetration in them. When this was observed, our group decided to measure the statistical properties of the avalanches, to see if they were repeatable and to compare their properties with the well-known dendritic avalanches caused by thermomagnetic instability.

It is shown that the critical state in such films in some samples is built up via a flux avalanches satisfying a power-law size distribution. Relaxations in the form of flux avalanches after the field has been stabilized for several seconds are also seen. The avalanches are not repeatable and thus not a deterministic result of defects, instead the critical state is built up by a stochastic process. They also never overtake the flux front substantially and show no threshold fields. It is therefore argued that the avalanches are not of thermomagnetic origin and a better explanation is that they are non-thermal rearrangements of the flux line lattice. Interestingly, the measured data fits nicely into the framework of self-organized criticality (SOC), a scenario which has attracted a lot of interest since 1987.

In paper 2, 3 and 4, I participated in theoretical discussions, experimental work and data analysis.

Paper 5 examines the differences in critical current between an ordinary YBCO film and a YBCO film deposited on a substrate covered with gold nanoparticles. It is always interesting to try to improve the strength of pinning in superconducting materials in order to increase the critical current. Artificial defects creating additional pinning sites can be introduced by several methods. Tilted substrates has already been mentioned, another one is deposition on a substrate covered with nanoparticles. It is shown that the YBCO films deposited on gold nanoparticles gets enhanced critical currents when compared to an ordinary YBCO film. Also, an ageing effect is seen. The YBCO films deposited on nanoparticles get enhanced critical currents at low applied fields as they age, while the critical current is reduced at high applied fields, compared to an ordinary YBCO film. My contribution to this work was the magneto-optical images of flux penetration.

Paper 6 is about flux pinning in a superconducting pnictide (Ba,K)Fe_2As_2. Since the discovery of superconductivity in iron-based pnictides in 2006, there has been a significant interest in investigating this large class of materials. They are considered to be HTS materials and there has been hope that a second class of HTS materials can help explain the mechanism behind superconductivity in the cuprate materials known from 1986. They might also be better suited for certain applications due to a combination of relatively high critical temperatures and better mechanical properties than the superconducting cuprates. It is thus of interest to determine sample quality, critical current and whether there are flux avalanches in these materials. Magneto-optical studies of pnictide materials will become even more relevant for these tasks in the near future, as thin-films of high quality are starting to be produced.

My contribution to this paper was taking part in the magneto-optical measurements which revealed a good, uniform sample quality. With this data, the critical current density as a function of temperature at low applied magnetic fields was determined. Another result in this paper is the presence of flux avalanches in an iron-based pnictide superconductor, a new result (this result was extracted from magnetization measurements on a large sample by our collaborators).

Outlook

There are several more questions relating to this work that remain unanswered:

- What are the conditions for having non-thermal flux avalanches in a superconductor? What determines whether the critical state is built up smoothly or through avalanches? Simulations show several kinds of size distributions of the avalanches, both power laws and peaked distributions. Many simulations do however not correspond very well to what is, or can be, experimentally seen with magneto-optics. It is hard to deduce the spatial shape and the fractal dimension of avalanches with integral measurements. Thus, magneto-optical imaging continues to be ideally suited for investigating such topics. Much work remains to be done here, this work should also include single-vortex imaging.

- Vortices in superconductors are potentially an ideal system for investigating SOC, as they are usually thought to be massless. In piles of sand or rice, inertial effects might destroy SOC. What can we learn about the SOC framework from investigating superconductors? When is it applicable? When is it not?

- Studies of different YBCO samples on tilted substrates show that both smooth and intermittent penetration in one-dimensional channels are possible behaviors. Also, at high temperatures, there are no avalanches in any of these samples. The avalanches are believed to be caused by clogging of flux bundles in the channels. Clogging effects are more pronounced in lower dimensions for obvious reasons. To investigate the topics mentioned above, one could artificially pattern samples with one-dimensional channels of strong and weak pinning and vary their spacing, relative pinning strengths etc. Then one would have more control over the parameters leading to smooth or intermittent behavior, facilitating theoretical explanations. Another topic could be to pattern samples with regularly spaced edge defects to serve as points of easier flux penetration. Will there be non-thermal avalanches nucleating from such defects?

- What is the interplay between non-thermal flux avalanches and large, thermomagnetic avalanches giving rise to dendrites? Simulations indicate that the ramping rate must be very high in order to trigger dendrites. However, experiments show that dendrites will appear even if the ramping rate is extremely slow. Clogging of vortices with subsequent breakthroughs and abrupt flux movement is a likely candidate to explain this. This means that the micro-structure of samples is important for its thermomagnetic stability. A work showing that NbN samples with less microscopic disorder are thermomagnetically stable, while films with more disorder are unstable is nearing completion in our group.

- Several works indicate a strong suppression of dendrites by a metal layer on top of the sample. A preliminary experiment indicated that there was no visible suppression of the flux avalanches in the series of YBCO samples on tilted substrates. One should make such samples with metal coating to investigate this problem quantitatively, though one must make sure that the deposition of metal does not degrade the superconducting material.

- Are there dendrites in iron-based pnictide superconductors and can they be seen by magneto-optics? HTS materials like YBCO do not show them unless externally triggered. Paper 6 indicates that there at least exist large flux avalanches in an iron-based pnictide material, though their origin is less clear.

- Magneto-optics with fast cameras. Dendrites propagate so fast that their growth cannot be seen with any existing fast camera, but the growth of non-thermal flux avalanches appears from a preliminary study to be much slower. It might for example be possible to see whether the waiting times between such events obey power-law statistics, another prediction of the SOC framework.
- Magneto-optical indicator garnets with in-plane magnetization are usually limited for application to below $B = 100$ mT, as the Faraday rotation saturates. At least one series of experimental indicator films had a saturation field much higher than this, around $B = 200$ mT. How far is it possible to push this limit?

In other words, there is plenty of work to do in this area for both the experimentalist and the theorist in the coming years!

List of papers

Paper 1 *Irreversibility of the threshold field for dendritic flux avalanches in superconductors*
A. J. Qviller, V. V. Yurchenko, K. Eliassen, J. I. Vestgården,
T. H. Johansen, M. R. Nevala, I. J. Maasilta, K. Senapati,
R. C. Budhani

Published, Physica C **470**, 897 − 900, (2010).

Paper 2 *Anisotropic currents and flux jumps in high-T_c superconducting films with self-organized arrays of planar defects*
V. V. Yurchenko, A. J. Qviller, P. B. Mozhaev, J. E. Mozhaeva,
J. B. Hansen, C. S. Jacobsen, I. M. Kotelyanskii, A. V. Pan,
T. H. Johansen

Published, Physica C **470**, 799 − 802, (2010).

Paper 3 *Intermittent Flux Penetration at Different Temperatures in $YBa_2Cu_3O_{7-x}$ on $NdGaO_3$ Substrates*
A. J. Qviller, V. V. Yurchenko, J. I. Vestgården, T. H. Johansen,
Y. Galperin, P. B. Mozhaev, J. E. Mozhaeva, J. B. Hansen,
C. S. Jacobsen

Published, J. Supercond. Nov. Magn. **24**, 179 − 181, (2011).

Paper 4 *Quasi-One-Dimensional Intermittent Flux Behavior in Superconducting Films*
A. J. Qviller, V. V. Yurchenko, Y. M. Galperin, J. I. Vestgården,
P. B. Mozhaev, J. B. Hansen, T. H. Johansen

Published, Phys. Rev. X. **2**, 011007, (2012). The paper has supplementary material in the form of videos which can be accessed online.

Paper 5 *Magneto-optical imaging of columnar YBCO films*
P. Mikheenko, V. V. Yurchenko, J. L. Tanner, A. J. Qviller,
Y. M. Galperin, J. I. Vestgården, A. Crisan, T. H. Johansen

Accepted for publication in Physics Procedia.

Paper 6 *Very strong intrinsic flux pinning and vortex avalanches in (Ba,K)Fe_2As_2 superconducting single crystals*

Xiao-Lin Wang, S. R. Ghorbani, Sung-Ik Lee, S. X. Dou, C. T. Lin,
T. H. Johansen, K. H. Müller, Z. X. Cheng, G. Peleckis, M. Shabazi,
A. J. Qviller, V. V. Yurchenko, G. L. Sun, and D. L. Sun

Published, Phys. Rev. B **82**, 024525, (2010).

J Supercond Nov Magn (2011) 24: 179–181
DOI 10.1007/s10948-010-0915-5

ORIGINAL PAPER

Intermittent Flux Penetration at Different Temperatures in $YBa_2Cu_3O_{7-x}$ on $NdGaO_3$ Substrates

**Atle Jorstad Qviller · Vitaliy Yurchenko ·
Jørn Inge Vestgården · Tom Henning Johansen ·
Yuri Galperin · Peter B. Mozhaev · Julia E. Mozhaeva ·
Jørn Bindslev Hansen · Claus Schelde Jacobsen**

Received: 7 September 2010 / Accepted: 9 September 2010 / Published online: 6 October 2010

Abstract In type-II superconductors, increasing applied magnetic field penetrates gradually in the form of magnetic vortices. It is of great interest to understand the dynamics of magnetic flux in different superconducting materials, as this phenomenon can severely limit the performance of superconductors in applications. $YBa_2Cu_3O_{7-x}$ (YBCO) is an important high-temperature superconductor, but until recently, it has been hard to make wires from it due to misalignment of superconducting grains. A solution to this problem is to deposit YBCO on vicinal substrates to better align the grains. Some of these samples show a strongly intermittent flux penetration at low temperatures. In this work, we have studied flux penetration in YBCO deposited on a 14° vicinal substrate of $NdGaO_3$ (NGO) at different temperatures.

Keywords Flux avalanches · Thermomagnetic instability · Magneto-optical imaging · Miscut substrate · Vicinal substrate

1 Introduction

The interest in high-temperature superconducting cuprates deposited on tilted (miscut, vicinal) substrates was originally motivated by improved alignment of grains, resulting in higher transport currents [1]. Also, the possibility to manufacture Josephson junctions with arbitrary tilt angles (TOP-junctions) from these films has become another motivating factor [2]. Films of $YBa_2Cu_3O_{7-x}$ (YBCO) grown on tilted substrates differ in several respects from YBCO films grown on flat substrates, as anti-phase boundaries (APBs) are introduced in the film along the substrate microsteps. Flux penetration is therefore anisotropic, resulting from different critical currents longitudinal (L) and transverse (T) to the APBs; see [1] for details. Instead of a smooth flux front, flux penetrates more easily in filaments along extended defects along the L-direction.

2 Experimental

2.1 Samples

By laser ablation of stochiometric targets, films of YBCO were deposited on $NdGaO_3$ (NGO) substrates with different miscut angles. The temperature during the deposition was 800 °C and the beam energy density 1.5 J/cm^2 in a surrounding atmosphere of 20% oxygen content and a pressure of 0.8 mbar. Selected for the present measurements was a film grown on a 14° miscut substrate. The superconducting film has a thickness of 150 nm. Detailed information about the sample preparation can be found in [3].

A.J. Qviller (✉) · V. Yurchenko · J.I. Vestgården ·
T.H. Johansen · Y. Galperin
Department of Physics, University of Oslo, Oslo, 0316, Norway
e-mail: atleq@fys.uio.no

P.B. Mozhaev · J.E. Mozhaeva · J.B. Hansen · C.S. Jacobsen
Department of Physics, Technical University of Denmark,
Kgs.Lyngby, 2800, Denmark

P.B. Mozhaev · J.E. Mozhaeva
Institute of Physics and Technology RAS, Moscow, 117218,
Russia

2.2 Magneto-Optical Measurements

A Leica polarized light microscope and a Faraday active ferrite garnet indicator film placed on top of the sample mounted in an Oxford Microstat continuos flow cryostat constitutes the setup used for magneto-optical imaging. A Delta Elektronika power supply and a pair of coils provided external magnetic fields in the range $B = 0$ mT to $B = 85$ mT. With the help of an Oxford temperature controller, the sample was cooled to $T = 5$ K in one experiment and $T = 15$ K in another. At both of these temperatures, the external field was ramped up from zero to 21.25 mT, with field steps of $\Delta B = 4.25$ μT. Images were captured by a RetigaExi camera at every tenth step. Four series of images were recorded at both temperatures. A series of images was also recorded just above the sample T_c of 90 K in order to calibrate the light intensity response of the indicator film. By combining these measurements, quantitative magnetic field values were extracted from the magneto-optical images.

2.3 Image Analysis of Jumps

In Fig. 1, a magneto-optical image of the sample in an applied field of 17 mT at $T = 8$ K is shown as an in-set in the upper panel.[1] The main panel of Fig. 1 shows the part of the image marked by a rectangular window, and gives a magnified view to clearly show the structure of flux filaments transverse to the strip direction. The lower panel of Fig. 1 shows a *differential image* created by subtracting two images taken at subsequent field steps. Bright regions correspond to increased flux density and dark regions correspond to decreased flux density. It is evident that the flux invades the film in a non-uniform way, in the form of quasi 1-dimensional filaments.

In order to make a statistical analysis of the flux jumps, the differential images were subjected to a median filter and converted into binary images defined by a threshold intensity. Every pixel with an intensity value below this threshold was given the color black, every pixel above was given the color white. A MATLAB algorithm was then used to identify the jumps and put a rectangular box around each of them. By superposing these boxes on the original image, the total number of flux quanta in each jump and the spatial dimensions of each jump were calculated. Different median filters and thresholds were tried and the resulting distributions converged for flux jump sizes larger than about $50\varphi_0$. The size distributions of jumps appear insensitive to the field step size, as $\Delta B = 42.5$ μT and $\Delta B = 25.5$ μT have resulted in nearly identical size- and length distributions of jumps.

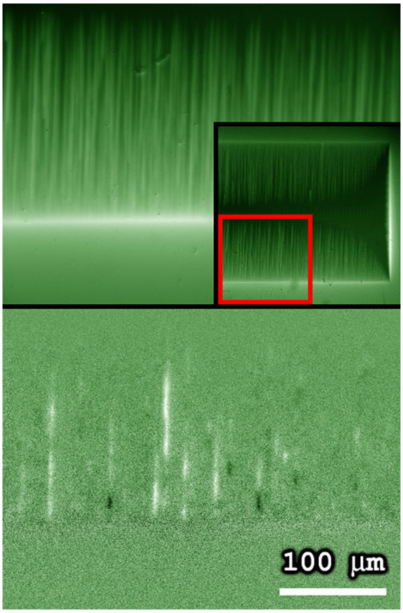

Fig. 1 (Color online) *Upper panel in-set*: The sample at $T = 8$ K, $B = 17$ mT. *Upper panel*: Magneto-optical image, $T = 8$ K, $B = 17$ mT. *Lower panel*: Differential image. $T = 8$ K, $B = 17$ mT and $\Delta B = 42.5$ μT.

3 Results and Analysis

In earlier experiments [1], a pattern of flux filaments has been seen in YBCO deposited on $SrTiO_3$ (STO) samples with a miscut angle of 9.5°. These filaments are also present in YBCO samples deposited on NGO substrates, as visible in Fig. 1, top. They originate from the edge of the superconducting sample, which is seen as the bright, horizontal line in Fig. 1, top. The in-set shows that filaments are only present in one direction, which is longitudinal to the microsteps of the substrate. Filaments are most visible below $T = 30$ K and more pronounced at lower temperatures. At higher temperatures, the flux motion is non-intermittent in both directions and no filaments are seen. At temperatures below $T = 30$ K, the flux motion become intermittent in the direction longitudinal to the substrate microsteps. There is still a smooth background flow of flux in this direction, but now, entire flux bundles displace collectively, as can be seen in Fig. 1, bottom. There are never jumps in the direction transverse to the microsteps of the substrate. The appearance of the flux jumps has a similar temperature dependence as the filaments, they are better defined at low temperatures, and become more and more smeared out at higher temperatures, disappearing at about $T = 30$ K.

Figure 2 shows the length-distribution of jumps at $T = 5$ K and $T = 15$ K temperatures, occuring as the applied

---

[1] A strange anisotropy of the flux penetration in this sample is here evident.

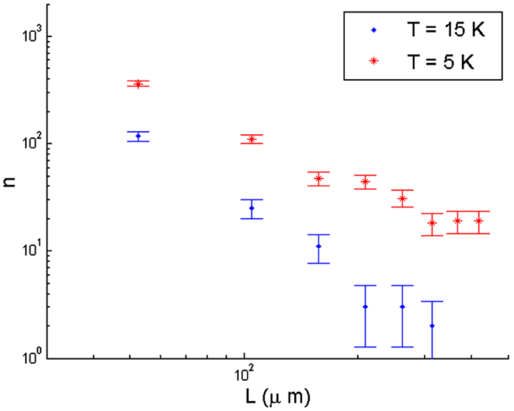

Fig. 2 (Color online) Length of flux jumps at $T = 5$ K and $T = 15$ K

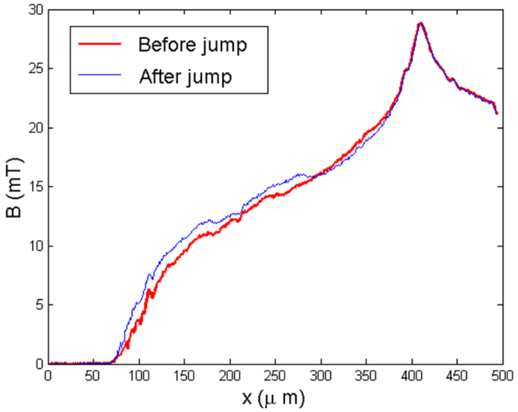

Fig. 3 (Color online) The field profiles before and after a relaxation occuring at $B = 17$ mT

magnetic field was increased from $B = 19.25$ mT to $B = 21.25$ mT in four different measurement runs at each temperature. It is evident that much fewer jumps of a given length are seen at the higher temperature. Otherwise, the statistical distributions have a similar shape. So far we have not found clear kinks or extrema in the distributions, indicating no characteristic size or length of the flux jumps in a wide range of fields.

Flux relaxations is an important phenomenon in high temperature superconductors and the effect often manifests itself as a smooth flux creep. In order to check whether our sample also showed relaxations of an abrupt kind, we performed the following experiment: The magnetic field was increased from $B = 0$ mT to $B = 17$ mT in a single step and then held at the latter value. Most flux jumps occurred immediately, while a few jumps occurred several seconds after the field increase. Shown in Fig. 3 are flux profiles before and after a flux jump happening at constant externally applied field. A redistribution of flux has occurred, but the magnetic field has changed very little at the flux front and at the edge of the sample.

4 Conclusions

Flux filaments and an intermittent flux penetration were seen in a YBCO sample deposited on a 14° miscut NGO substrate. The flux jumps were identified and statistics of their lengths were collected. At higher temperatures, the jumps are gradually disappearing by getting more smeared out. As a result, there are fewer jumps, though the shape of the length distributions of jumps are similar. Abrupt flux relaxations also occur in this sample.

References

1. Jooss, Ch., Warthmann, R., Kronmuller, H.: Phys. Rev. B **61**, 18 (2000)
2. Tafuri, F., et al.: Physica C **326**, 63 (1999)
3. Mozhaev, P.B., et al.: Physica C **435**, 23 (2006)

PHYSICAL REVIEW X 2, 011007 (2012)

Quasi-One-Dimensional Intermittent Flux Behavior in Superconducting Films

A. J. Qviller,[1] V. V. Yurchenko,[1] Y. M. Galperin,[1,2,3] J. I. Vestgården,[1] P. B. Mozhaev,[4,5]
J. B. Hansen,[4] and T. H. Johansen[1,3,6]

[1]*Department of Physics, University of Oslo, P.O. Box 1048 Blindern, 0316 Oslo, Norway*
[2]*Ioffe Physical Technical Institute of the Russian Academy of Sciences, 194021 St. Petersburg, Russia*
[3]*Centre for Advanced Study at the Academy of Science and Letters, 0271 Oslo, Norway*
[4]*Department of Physics, Technical University of Denmark, Kongens Lyngby, DK-2800, Denmark*
[5]*Institute of Physics and Technology of the Russian Academy of Sciences, Moscow, 117218, Russia*
[6]*Institute for Superconducting and Electronic Materials, University of Wollongong,*
Northfields Avenue, Wollongong, New South Wales 2522, Australia

(Received 16 June 2011; published 27 January 2012)

Intermittent filamentary dynamics of the vortex matter in superconductors is found in films of $YBa_2Cu_3O_{7-\delta}$ deposited on tilted substrates. Deposition of this material on such substrates creates parallel channels of easy flux penetration when a magnetic field is applied perpendicular to the film. As the applied field is gradually increased, magneto-optical imaging reveals that flux penetrates via numerous quasi-one-dimensional jumps. The distribution of flux avalanche sizes follows a power law, and data collapse is obtained by finite-size scaling, with the depth of the flux front used as crossover length. The intermittent behavior shows no threshold value in the applied field, in contrast to conventional flux jumping. The results strongly suggest that the quasi-one-dimensional flux jumps are of a different nature than the thermomagnetic dendritic (branching) avalanches that are commonly found in superconducting films.

DOI: 10.1103/PhysRevX.2.011007 Subject Areas: Materials Science, Statistical Physics, Superconductivity

Since the prediction of a regular vortex lattice in type-II superconductors [1], a wide variety of vortex systems has been thoroughly investigated [2,3]. The pronounced dependencies of the range and strength of the vortex-vortex interaction on temperature and magnetic field make the vortex matter a unique, tunable model system for probing the statistical properties of interacting systems. The behavior of the vortex matter is to a large extent also determined by its interaction with quenched disorder in the material, i.e., with microscopic defects that pin the vortices and therefore serve as pinning centers in the superconductor. The interplay between the pinning forces and the driving Lorentz force leads to formation of a metastable critical state [4], where the current density has a critical magnitude, j_c, which corresponds to the maximal nondissipative current density.

In films of $YBa_2Cu_3O_{7-\delta}$ (YBCO) grown epitaxially, i.e., with proper matching of crystal lattice parameters, on a substrate slightly tilted from a major crystal plane (vicinal films), self-organized arrays of planar defects (antiphase boundaries) are formed with a typical period of 2–5 nm [5]. The terrace structure of the surface is characterized by steps that are a few Ångströms in height, and the steps provide well-oriented seeding sites for growth along the main axis (c axis) of the overlying YBCO film. Films grown on substrates with a tilt angle of θ close to 10° have better grain alignment and improved current-carrying ability [5,6]. There has been considerable interest in such films due to their potential application in Josephson-junction design [7–9], in particular for highly sensitive detectors of electromagnetic radiation.

The growth of YBCO films on tilted substrates is also known to produce planar defects, which become channels for easy vortex motion [5,6,10]. These channels are separated by 5–10 μm and run parallel to the terrace structure, causing considerable anisotropy in both the flux penetration and the effective critical current. At low temperatures, where the anisotropy is most pronounced, the vortices are essentially confined inside the channels, and the flux penetration has a strong quasi-one-dimensional (quasi-1D) character. In this paper, we show, using magneto-optical imaging (MOI), that the quasi-1D flux dynamics is highly intermittent at low temperatures in samples with moderate tilt angles.

Intermittent flux motion is very harmful for electronic devices, so the source of intermittency should be identified and the behavior characterized. Until now, intermittent flux behavior in superconducting films has been observed in Nb, Pb, Nb_3Sn, NbN, MgB_2, and YNi_2B_2C [11–16], where, during slow ramping of the applied field, the flux avalanches take the form of large dendritic (branching) structures. These avalanches are believed to be caused by a thermomagnetic instability [17–20]. We find that, in YBCO on tilted substrates, the flux jumps are largely

---

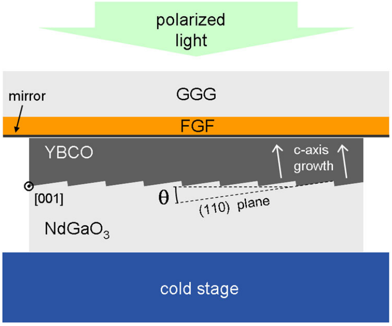

FIG. 1. Mounting in the cryogenic MOI setup of the YBCO film on a NdGaO substrate with a terrace-structured surface. Also shown is the orientation of the crystallographic axes specified by Miller indices, as well as the tilt angle θ. On top of the superconductor is the Faraday rotating ferrite-garnet film (FGF), grown on a gadolinium-gallium-garnet (GGG) substrate, which allows realtime visualization of the flux density across the film area.

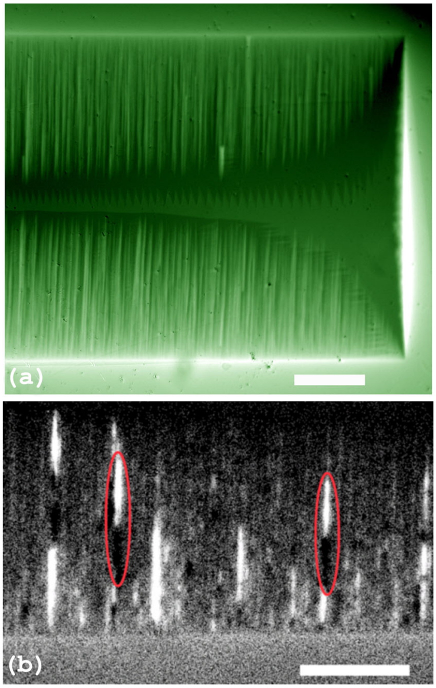

FIG. 2. (a) Direct and (b) differential magneto-optical images of flux penetration in a YBCO film on a $\theta = 14°$-tilted substrate. The applied magnetic field is $B_a = 16.2$ mT, and the sample temperature is $T = 4$ K. The image brightness represents the distribution of flux density. In (b), the linear streaks show the avalanches taking place during $\Delta B_a = 42.5$ μT. The white scale bars at the bottom of each panel are 200 μm long.

different from the thermomagnetic avalanches both in morphology and in size distribution, suggesting that the origin of the intermittency is of a different nature.

Superconducting films are prepared by laser ablation (vaporization by a laser beam and subsequent crystallization) of $YBa_2Cu_3O_{7-\delta}$ ceramic targets on $NdGaO_3$ substrates with tilt angles θ of up to 33°. (See Ref. [9] for sample preparation details.) The films we investigate in the present work have thickness of $d = 200$ nm and a critical temperature of $T_c = 88$ K. They are shaped by optical lithography into long strips of width $2w = 0.9$ mm. Low-temperature MOI is performed using an in-plane magnetized ferrite-garnet film as the Faraday rotating sensor [21,22]. The measurement configuration is illustrated in Fig. 1.

Figure 2(a) shows a magneto-optical image of the flux penetration in a $\theta = 14°$ film where the surface steps are aligned vertically in the picture. The sample is initially cooled to $T = 4$ K at zero field, and then a perpendicular applied magnetic field is slowly increased at a rate of $0.2\ \mathrm{mT}/s$. The image is recorded at $B_a = 16.2$ mT. The flux penetrates the sample from the two long edges, seen in the figure as bright horizontal lines, in a distinctly filamentary manner, where the filaments are aligned with the underlying terrace steps. From the short edge, however, the flux penetration is essentially blocked by the strong pinning associated with vortex motion transverse to the terrace structure. The full flux dynamics during such a field ramp is seen in Video 1.

From the real-time observation, it is evident that the penetration is strongly intermittent, where the flux enters from both long edges via discrete quasi-1D avalanches. This penetration is also documented in panel (b) of Fig. 2,

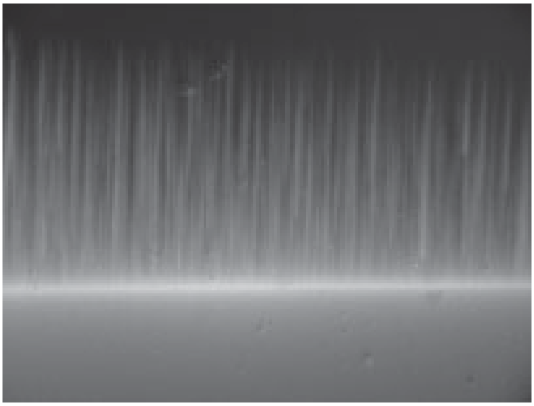

VIDEO 1. The intermittent flux penetration in the YBCO film shown in Figure 2. Needlelike flux avalanches are seen as abrupt events as the magnetic field B_a is increased from zero to 17 mT in steps of $\Delta B_a = 42.5$ μT. The sample temperature is $T = 8$ K.

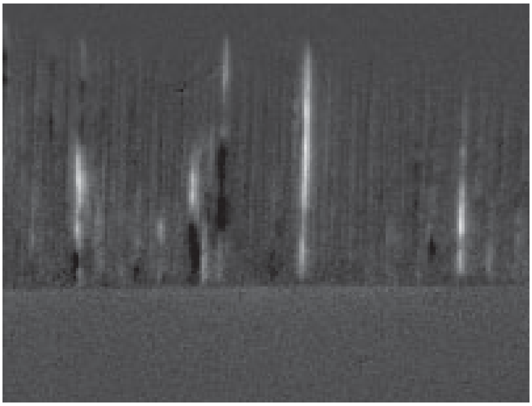

VIDEO 2. The differential video obtained by subtracting subsequent frames in Video 1.

which shows the result of subtracting two subsequently recorded images. The bright streaks show the abrupt arrival of the flux entering either (i) from the edge where new vortices nucleate, or (ii) from an internal vortex rearrangement [23]. The red ovals in the figure mark examples of internal avalanches, whereas the dark streaks are the regions from which the flux escaped. All this dynamics takes place within a field interval of only $\Delta B_a = 42.5\ \mu$T. A differential movie of the flux dynamics is included as Video 2. Analyzing the sequence of avalanches from such movies, we find no correlation between flux jumps in adjacent channels. Thus, the overall flux-penetration process can be considered as a sequence of independent avalanche events.

More insight into the phenomenon is obtained by determining whether the avalanches are reproducible or not. The well-known dendritic flux avalanches caused by thermomagnetic instability have the characteristics of being irreproducible [15,24,25]. When a field sweep is repeated under the same experimental conditions, the flux patterns show essentially no overlap, suggesting that stochastic fluctuations play a main role. The present quasi-1D avalanches also display irreproducible behavior, although on a smaller scale. Figure 3 shows a superposition of three monochrome color-coded (red, green, and blue) differential images taken at the same applied field and temperature during three different consecutive experimental runs. In an image made in this way, repeatable features appear as a gradation of gray for repeatable features, whereas events that occur in only one run appear as red, green, or blue. The superposition is black in areas where no flux change occurs in any of the images. Evidently, there is no overlap in the three sets of flux avalanches [26]. The same irreproducibility has been found at all fields investigated.

All the quasi-1D avalanches are limited in length by the overall flux-penetration front as it advances toward the middle of the strip in response to the increasing applied magnetic field. The front is built up as an envelope of numerous flux needles formed by the avalanches penetrating the most deeply into the film. This result is strikingly different from the dendritic type of avalanches, where the size of the jumps can span the sample even with a small applied field, and the flux front in general attains a very complex shape. In our case, the flux front is far more well behaved.

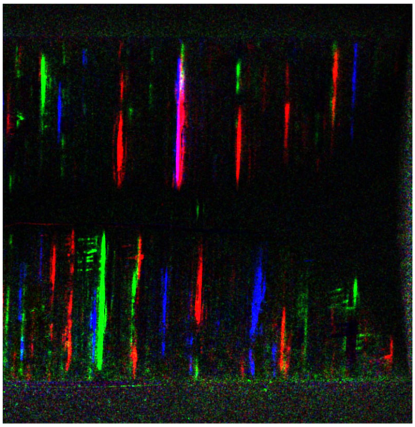

FIG. 3. Superposition of three magneto-optical differential images of flux penetration in a YBCO film on a $\theta = 14°$-tilted substrate. The different monochrome image series are color coded in red, green, and blue, respectively. The presence of colored superpositions shows that the flux jumps are not reproducible. The sample temperature is $T = 4$ K, the applied magnetic field is $B_a = 16.7$ mT, and the field step is $\Delta B_a = 42.5\ \mu$T. The scale is the same as for Fig. 2(a).

To quantify the new type of intermittent flux dynamics, we record magneto-optical images while the applied field

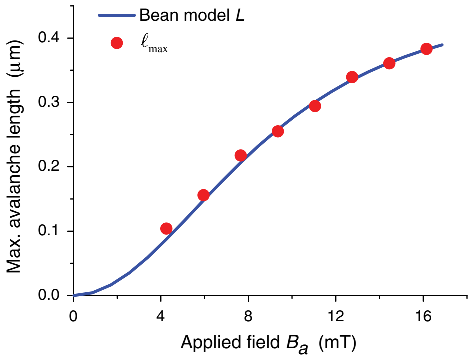

FIG. 4. Dependence of the maximum avalanche length, $\ell_{\max}$, on the applied field (red dots). The solid blue curve shows the Bean-model flux penetration depth, L, given by Eq. (1).

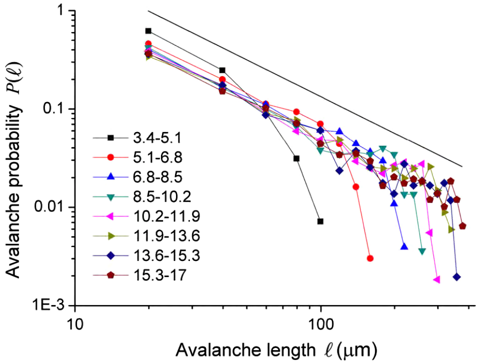

FIG. 5. Statistics of avalanche length, ℓ, observed while the applied field is ramped from zero to $B_a = 17$ mT in steps of $\Delta B_a = 42.5\ \mu$T. The curves correspond to the field intervals listed in the key (mT). The straight line with a slope of -1.3 is added as a guide to the eye.

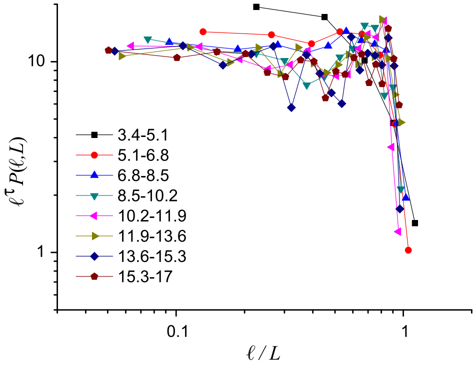

FIG. 6. Collapse of the data in Fig. 5, showing finite-size scaling. The graphs correspond to the field intervals listed in the key (mT).

is slowly ramped from zero to $B_a = 17$ mT. The sample becomes nearly fully penetrated by flux. Images are recorded every 42.5 μT. From all these images, a sequence of difference images is prepared, and, for every avalanche that occurs, its length ℓ is measured by using a pattern-recognition program. Figure 4 shows how $\ell_{\max}$, the size of the longest avalanche within each field interval, varies with the applied field. The maximum length follows a smooth curve, which corresponds very well to the advancement of the overall flux front, i.e., at all fields, there are avalanches starting at the edges and ending at the flux front. Actually, the $\ell_{\max}(B_a)$ behaves in full accord with the flux-penetration depth for a long thin superconducting strip in the critical state. For a strip in the Bean critical state, the flux front reaches a depth of L given by [27]

$$L/w = 1 - \cosh^{-1}(B_a/B_d), \tag{1}$$

where $B_d = \mu_0 j_c d/\pi$. In Fig. 4, $L(B_a)$ is plotted to fit the experimental data using a critical current density of $j_c = 0.78 \times 10^{11}\ \mathrm{Am}^{-2}$ as the only fitting parameter. Based on the good agreement, we conclude that the overall flux front evolves with the applied field according to the conventional critical-state behavior, whereas the detailed dynamics is governed by quasi-1D flux avalanches of length up to the depth of the flux front.

Figure 5 shows the size distribution of all the detected avalanches of more than 10 000, as a normalized probability for the occurrence of an avalanche of length ℓ. The data are grouped into equal field intervals of 1.7 mT. From the log-log plot, it is evident that the vast majority of the avalanches are distributed as a power law $P(\ell) \sim \ell^{-\tau}$. The avalanche distribution has a natural cutoff length at the overall flux-penetration depth $L(B_a)$. A fit to the linear part of the data gives $\tau = 1.3$ for the exponent. Applying finite-size scaling according to the relation

$$\mathcal{P}(\ell, L) \propto \ell^{-\tau} f\left(\frac{\ell}{L^D}\right), \tag{2}$$

where f is a scaling function, the plot in Fig. 6 shows that a good data collapse is obtained with $D = 1$.

To summarize the experimental results, we have found that, at small fields, the avalanches are also small, and, as the applied field becomes larger, the maximum avalanche size gradually increases. The envelope curve of the flux-penetration front is slightly ramified (split into branches) by the avalanche activity, but it still behaves essentially in full accord with the critical-state model. Analyzing avalanches that occur within a small field interval as the applied field increases, we find that the distribution of

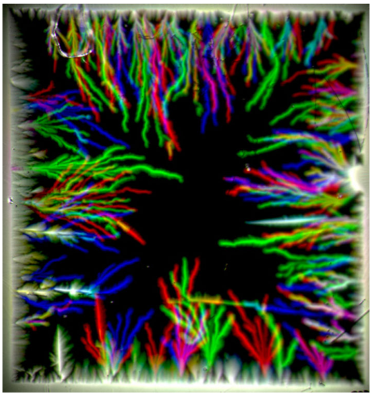

FIG. 7. Superposition of three magneto-optical images (red, green, and blue) taken at the same applied field, $B_a = 22$ mT at $T = 9.2$ K in three different experimental runs. The presence of colors shows that the dendritic avalanches are irreproducible. The sample is a $5 \times 5\ \mathrm{mm}^2$, 300-nm-thick film of MgB_2 on Al_2O_3 $(1\bar{1}02)$ substrate.

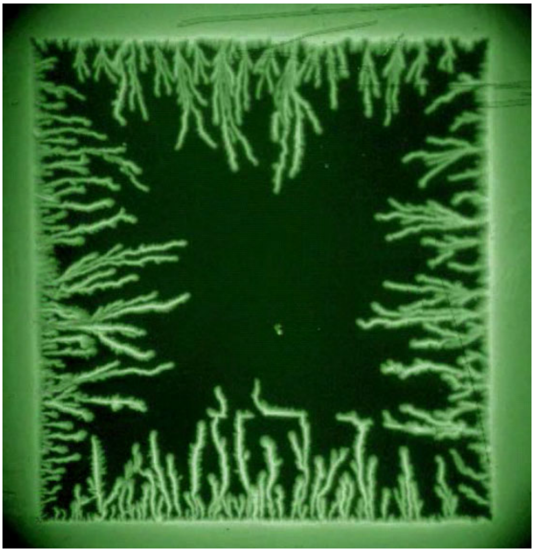

VIDEO 3. For comparison, a typical set of flux avalanches in a MgB_2 film. Notice the different morphology between these avalanches spanning the sample in complex dendritic patterns, and those seen in Video 1.

avalanche sizes is a monotonously decreasing curve. All these characteristics are in stark contrast to the observations reported for flux avalanches caused by thermomagnetic runaways. Figure 7 illustrates the typical dendritic morphology of the thermomagnetic-runaway type of avalanches, here seen in a film of MgB_2. A movie of the dendritic flux penetration into a film of MgB_2 is seen in Video 3. The avalanches protrude in highly nonregular shapes, deep into the Meissner-state part of the film, and histograms of the avalanche size show a strongly peaked distribution [28]. Moreover, in contrast to the dendritic avalanches, our observations of the present YBCO films do not detect any threshold field for onset of the avalanche activity. Thus, there are several significant differences between the two types of avalanches, which suggest that the quasi-1D flux jumps in YBCO on tilted substrates are not of a thermomagnetic origin.

A more likely scenario is that the intermittent filamentary behavior is a result of vortex dynamics under conditions of channeling, which is clearly seen in the current MOI experiments. The film has a large number of linear defects which form parallel narrow channels with low pinning surrounded by areas of strong pinning, thus providing quasi-1D confinement. As flux enters these channels, some vortices will also penetrate into the strong-pinning areas, thus forming a fence on both sides. These vortices, which sit at strong-pinning sites, certainly will have substantial positional disorder and hence add a considerable random component to the confinement. Thus, the channels will contain a sequence of random bottlenecks for the traffic of vortices. As the applied magnetic field increases, more and more vortices penetrate into the channels, and situations analogous to a traffic jam, or clogging, will occur. Whenever one of these blocked regions eventually breaks open, an avalanche of vortex motion takes place along the channel. Since these barriers can be arbitrarily small, there is no threshold applied field for the onset of this intermittent behavior. This picture is consistent with our experimental observations. Moreover, this mechanism allows avalanches to start not only from the sample edge, but also from inside the channels, which is also in accordance with our observations. Interestingly, this scenario resembles the flux motion found in artificially created mesoscopic flow channels. (See Ref. [29] and references therein.)

It is also worth discussing our results within the framework of self-organized criticality (SOC). Although the first dynamical system shown to display SOC, the Bak-Tang-Wiesenfeld sand pile [30], does not exhibit SOC in one dimension, several similar algorithms with different toppling rules and intrinsic randomness do [31–33]. These models were invented to study numerically a mechanical quasi-1D dynamical system, the Oslo rice pile [34], which for certain types of rice grains displays SOC behavior. The numerical simulations give power-law avalanche-size distributions with exponents in the range of 1.3–1.6, depending on the details of the model. Our measured avalanche exponent falls within this range.

In the SOC literature, various definitions are used for the size of an avalanche: the number of sites being toppled, the amount of dissipated energy, the spatial extent of an avalanche, etc. In the present work, we have also performed an alternative statistical analysis where the avalanche size is taken to be the amount of the flux being abruptly displaced in each event, rather than the length of the filamentary jumps. This alternative analysis also leads to good scaling and a power-law exponent that agrees within 0.1 of that reported in this paper. Aegerter *et al.* [35] have also reported power-law statistics of flux avalanches in YBCO thin films deposited on plain substrates. Using MOI, they find the exponent τ close to ours. However, their observed avalanches are far from being one dimensional, having $D = 1.89$. Closer-to-one-dimensional motion has been observed in small bundles of vortices in superconductor films of tungsten by use of scanning microscopy [36]. However, the data were accumulated over periods of many minutes, showing very different time characteristics compared to our observations. Note that, in contrast to the previous flux-imaging experiments[35,36], the present MOI observations cover the avalanche activity of the entire flux pile, enabling us to perform finite-size scaling with the physical size of the pile L, instead of analyzing a small viewing window.

Worth noting in Fig. 6 is the slight overshoot in the curves near the cutoff length, L. Also, simulations

[31–33] show this feature, i.e., a small increase in the probability of having avalanches of maximum size, which is interpreted as a finite-size effect [31]. To our knowledge, this effect has not been observed experimentally before in vortex systems.

Since inertia can destroy SOC in mechanical systems [37], superconducting vortices, commonly considered as massless, indeed represent a very favorable candidate for SOC, and a lot of numerical simulation work has been reported on the topic [38–41]. In particular, the simulations for two-dimensional vortex motion in a slab [39] show SOC behavior with scaling and power-law distributions, including an overshoot similar to that in our data.

We also perform similar experiments on YBCO films using two other ramp rates: 0.12 mT/s and 0.02 mT/s. No significant qualitative or quantitative changes in the behavior are observed. Moreover, intermittent flux dynamics has also been observed in vicinal samples with tilt angles of $\theta = 8°$, $10°$, and $12°$. However, in films with $\theta = 3°$, $20°$, $26°$, and $33°$, we find, not abrupt flux motion, but rather a smooth penetration into the channels. A reference sample with zero-degree tilt angle has shown neither flux jumps nor channeling. More work is required to clarify the relationship between the sample morphology and flux dynamics in superconductor films grown on vicinal-cut substrates.

In conclusion, we find that a gradual injection of the magnetic flux into a system of well-defined channels may trigger quasi-1D vortex avalanches, the sizes of which are distributed by a power law with the avalanche exponent $\tau = 1.3$. Introducing the depth of the flux front as a dynamic length scale makes the distributions invariant.

We acknowledge fruitful discussions with V. M. Vinokur, C. Reichhardt, K. T. Tallakstad, K. J. Måløy, J. Bergli, and E. Altshuler. The substrates for the films were produced by I. M. Kotelyanskii. The kind assistance of J. E. Mozhaeva during the sample preparation is also greatly appreciated. This work was financially supported by the Norwegian Research Council.

[1] A. A. Abrikosov, *On the Magnetic Properties of Superconductors of the Second Group*, Zh. Eksp. Teor. Fiz. **32**, 1442 (1957);[*On the Magnetic Properties of Superconductors of the Second Group*, Sov. Phys. JETP **5**, 1174 (1957)].

[2] G. Blatter, M. V. Feigel'man, V. B. Geshkenbein, A. I. Larkin, and V. M. Vinokur, *Vortices in High-Temperature Superconductors*, Rev. Mod. Phys. **66**, 1125 (1994).

[3] E. H. Brandt, *The Flux-Line Lattice in Superconductors*, Rep. Prog. Phys. **58**, 1465 (1995).

[4] C. P. Bean, *Magnetization of High-Field Superconductors*, Rev. Mod. Phys. **36**, 31 (1964).

[5] Ch. Jooss, R. Warthmann, and H. Kronmuller, *Pinning Mechanism of Vortices at Antiphase Boundaries in* $YBa_2Cu_3O_{7-\delta}$, Phys. Rev. B **61**, 12433 (2000).

[6] A. Polyanskii, R. L. S. Emergo, J. Z. Wu, T. Aytug, D. K. Christen, G. K. Perkins, and D. Larbalestier, *Magneto-Optical Imaging and Electromagnetic Study of* $YBa_2Cu_3O_7$ *Vicinal Films of Variable Thickness*, Phys. Rev. B **72**, 174509 (2005).

[7] J. H. Kim and D. Youm, *Growth of Textured c-Axis Normal* $YBa_2Cu_3O_{7-\delta}$ *Thin Films on Yttria-Stabilized Zirconia Substrates with Crystalline Axes Tilted with Respect to the Surfaces*, Physica C (Amsterdam) **275**, 273 (1997).

[8] I. K. Bdikin, P. B. Mozhaev, G. A. Ovsyannikov, P. V. Komissinski, and I. M. Kotelyanskii, *Growth and Domain Structure of* $YBa_2Cu_3O_x$ *Thin Films and* $YBa_2Cu_3O_x/CeO_2$ *Heterostructures on Tilted* $NdGaO_3$ *Substrates*, Physica C (Amsterdam) **377**, 26 (2002).

[9] P. B. Mozhaev, J. E. Mozhaeva, I. K. Bdikin, I. M. Kotelyanskii, V. A. Lusanov, J. Bindslev Hansen, C. S. Jacobsen, and A. L. Kholkin, *Out-of-Substrate Plane Orientation Control of Thin* $YBa_2Cu_3O_x$ *Films on* $NdGaO_3$ *Tilted-Axes Substrates*, Physica C (Amsterdam) **434**, 105 (2006).

[10] M. Djupmyr, G. Cristiani, H.-U. Habermeier, and J. Albrecht, *Anisotropic Temperature-Dependent Current Densities in Vicinal* $YBa_2Cu_3O_{7-\delta}$, Phys. Rev. B **72**, 220507(R) (2005).

[11] C. A. Duran, P. L. Gammel, R. E. Miller, and D. J. Bishop, *Observation of Magnetic-Field Penetration via Dendritic Growth in Superconducting Niobium Films*, Phys. Rev. B **52**, 75 (1995).

[12] M. Menghini, R. J. Wijngaarden, A. V. Silhanek, S. Raedts, and V. V. Moshchalkov, *Dendritic Flux Penetration in* Pb *Films with a Periodic Array of Antidots*, Phys. Rev. B **71**, 104506 (2005).

[13] I. A. Rudnev, S. V. Antonenko, D. V. Shantsev, T. H. Johansen, A. E. Primenko, *Dendritic Flux Avalanches in Superconducting* Nb_3Sn *Films*, Cryogenics **43**, 663 (2003).

[14] I. A. Rudnev, D. V. Shantsev, T. H. Johansen, A. E. Primenko, *Avalanche-Driven Fractal Flux Distributions in* NbN *Superconducting Films*, Appl. Phys. Lett. **87**, 042502 (2005).

[15] D. V. Denisov, D. V. Shantsev, Y. M. Galperin, Eun-Mi Choi, Hyun-Sook Lee, Sung-Ik Lee, A. V. Bobyl, P. E. Goa, A. A. F. Olsen, and T. H. Johansen, *Onset of Dendritic Flux Avalanches in Superconducting Films*, Phys. Rev. Lett. **97**, 077002 (2006).

[16] S. C. Wimbush, B. Holzapfel, and Ch. Jooss, *Magnetic Instability in* YNi_2B_2C *Thin Films: Observation of Dendritic Flux Instabilities in Borocarbides*, J. Appl. Phys. **96**, 3589 (2004).

[17] E. Altshuler and T. H. Johansen, *Colloquium: Experiments in Vortex Avalanches*, Rev. Mod. Phys. **76**, 471 (2004).

[18] A. L. Rakhmanov, D. V. Shantsev, Y. M. Galperin, and T. H. Johansen, *Finger Patterns Produced by Thermomagnetic Instability in Superconductors*, Phys. Rev. B **70**, 224502 (2004).

[19] D. V. Denisov, A. L. Rakhmanov, D. V. Shantsev, Y. M. Galperin, and T. H. Johansen, *Dendritic and Uniform Flux Jumps in Superconducting Films*, Phys. Rev. B **73**, 014512 (2006).

[20] I. S. Aranson, A. Gurevich, M. S. Welling, R. J. Wijngaarden, V. K. Vlasko-Vlasov, V. M. Vinokur, and U. Welp, *Dendritic Flux Avalanches and Nonlocal Electrodynamics in Thin Superconducting Films*, Phys. Rev. Lett. **94**, 037002 (2005).

[21] L. E. Helseth, R. W. Hansen, E. I. Il'yashenko, M. Baziljevich, and T. H. Johansen, *Faraday Rotation Spectra of Bismuth-Substituted Ferrite Garnet Films with In-Plane Magnetization*, Phys. Rev. B **64**, 174406 (2001).

[22] P. E. Goa, H. Hauglin, Å. A. F. Olsen, M. Baziljevich, and T. H. Johansen, *Magneto-Optical Imaging Setup for Single Vortex Observation*, Rev. Sci. Instrum. **74**, 141 (2003).

[23] For comparison, similar experiments were carried out on a sample with $\theta = 0°$. Here, the flux dynamics always developed quite smoothly, and difference images similar to that in panel 2(b) showed just featureless noise from the CCD camera.

[24] V. V. Yurchenko, D. V. Shantsev, T. H. Johansen, M. R. Nevala, I. J. Maasilta, K. Senapati, and R. C. Budhani, *Reentrant Stability of Superconducting Films and the Vanishing of Dendritic Flux Instability*, Phys. Rev. B **76**, 092504 (2007).

[25] V. V. Yurchenko, T. H. Johansen, and Y. M. Galperin, *Dendritic Flux Avalanches in Superconducting Films*, Low Temp. Phys. **35**, 619 (2009).

[26] Notice the very faint colors along the edge, which are caused by the flux jumps perturbing the external field near the edge and are a result of the nonlocal electrodynamics of thin-film superconductors [19,27].

[27] E. H. Brandt, and M. Indenbom, *Type-II-Superconductor Strip with Current in a Perpendicular Magnetic Field*, Phys. Rev. B **48**, 12893 (1993); E. Zeldov, J. R. Clem, M. McElfresh, and M. Darwin, *Magnetization and Transport Currents in Thin Superconducting Films*, Phys. Rev. B **49**, 9802 (1994).

[28] D. V. Shantsev, A. V. Bobyl, Y. M. Galperin, T. H. Johansen, and S. I. Lee, *Size of Flux Jumps in Superconducting Films*, Phys. Rev. B **72**, 024541 (2005).

[29] R. Besseling, P. H. Kes, T. Dröse, and V. M. Vinokur, *Depinning and Dynamics of Vortices Confined in Mesoscopic Flow Channels*, New J. Phys. **7**, 71 (2005).

[30] P. Bak, C. Tang, and K. Wiesenfeld, *Self-Organized Criticality*, Phys. Rev. A **38**, 364 (1988).

[31] M. Bengrine, A. Benyoussef, F. Mhirech, and S. D. Zhang, *Disorder-Induced Phase Transition in a One-Dimensional Model of Rice Pile*, Physica A (Amsterdam), **272**, 1 (1999).

[32] L. A. N. Amaral and K. B. Lauritsen, *Energy Avalanches in a Rice-Pile Model*, Physica A (Amsterdam) **231**, 608 (1996).

[33] L. A. N. Amaral and K. B. Lauritsen, *Self-Organized Criticality in a Rice-Pile Model*, Phys. Rev. E **54**, R4512 (1996).

[34] V. Frette, K. Christensen, A. Malthe-Sørensen, J. Feder, T. Jøssang, and P. Meakin, *Avalanche Dynamics in a Pile of Rice*, Nature (London) **379**, 49 (1996).

[35] C. M. Aegerter, M. S. Welling, and R. J. Wijngaarden, *Self-Organized Criticality in the Bean State of* $YBa_2Cu_3O_{7-x}$ *Thin Films*, Europhys. Lett. **65**, 753 (2004).

[36] I. Guillamón, H. Suderow, S. Viera, J. Sesé, R. Córdoba, J. M. De Teresa, and M. R. Ibarra, *Direct Observation of Stress Accumulation and Relaxation in Small Bundles of Superconducting Vortices in Tungsten Thin Films*, Phys. Rev. Lett. **106**, 077001 (2011).

[37] C. Prado and Z. Olami, *Inertia and Break of Self-Organized Criticality in Sandpile Cellular-Automata Models*, Phys. Rev. A **45**, 665 (1992).

[38] C. Reichhardt, C. J. Olson, J. Groth, S. Field, and F. Nori, *Microscopic Derivation of Magnetic-Flux-Density Profiles, Magnetization Hysteresis Loops, and Critical Currents in Strongly Pinned Superconductors*, Phys. Rev. B **52**, 10441 (1995); *Vortex Plastic Flow, Local Flux Density, Magnetization Hysteresis Loops, and Critical Current, Deep in the Bose-Glass and Mott-Insulator Regimes*, Phys. Rev. B **53**, R8898 (1996).

[39] K. E. Bassler and M. Paczuski, *Simple Model of Superconducting Vortex Avalanches*, Phys. Rev. Lett. **81**, 3761 (1998).

[40] C. Reichhardt, J. Groth, C. J. Olson, S. Field, and F. Nori, *Spatiotemporal Dynamics and Plastic Flow of Vortices in Superconductors with Periodic Arrays of Pinning Sites*, Phys. Rev. B **54**, 16108 (1996); C. J. Olson, C. Reichhardt, and F. Nori, *Superconducting Vortex Avalanches, Voltage Bursts, and Vortex Plastic Flow: Effect of the Microscopic Pinning Landscape on the Macroscopic Properties*, Phys. Rev. B **56**, 6175 (1997).

[41] C. Reichhardt, C. J. Olson, and F. Nori, *Commensurate and Incommensurate Vortex States in Superconductors with Periodic Pinning Arrays*, Phys. Rev. B **57**, 7937 (1998); *Nonequilibrium Dynamic Phases and Plastic Flow of Driven Vortex Lattices in Superconductors with Periodic Arrays of Pinning Sites*, **58**, 6534 (1998).

PHYSICAL REVIEW B **82**, 024525 (2010)

Very strong intrinsic flux pinning and vortex avalanches in (Ba,K)Fe_2As_2 superconducting single crystals

Xiao-Lin Wang,[1,*] S. R. Ghorbani,[1,2] Sung-Ik Lee,[3,†] S. X. Dou,[1] C. T. Lin,[4] T. H. Johansen,[1,5] K.-H. Müller,[6] Z. X. Cheng,[1] G. Peleckis,[1] M. Shabazi,[1] A. J. Qviller,[5] V. V. Yurchenko,[5] G. L. Sun,[4] and D. L. Sun[4]
[1]*Institute for Superconducting and Electronic Materials, Faculty of Engineering, University of Wollongong, Wollongong, New South Wales 2522, Australia*
[2]*Department of Physics, Sabzevar Tarbiat Moallem University, P.O. Box 397, Sabzevar, Iran*
[3]*National Creative Research Initiative Center for Superconductivity, Department of Physics, Sogang University, Seoul 121-742, Republic of Korea*
[4]*Max Planck Institute for Solid State Research, Heisenbergstr 1, 70569 Stuttgart, Germany*
[5]*Department of Physics, University of Oslo, P.O. Box 1048, Blindern, 0316 Oslo, Norway*
[6]*CMSE, CSIRO, Lindfield, New South Wales 2070, Australia*
(Received 21 May 2010; published 28 July 2010)

We report that the (Ba,K)Fe_2As_2 crystal with $T_c=32$ K shows a pinning potential, U_0, as high as 10^4 K, with U_0 showing very little field dependence. The (Ba,K)Fe_2As_2 single crystals become isotropic at low temperatures and high magnetic fields, resulting in a very rigid vortex lattice, even in fields very close to H_{c2}. The isotropic rigid vortices observed in the two-dimensional (2D) (Ba,K)Fe_2As_2 distinguish this compound from 2D high-T_c cuprate superconductors with 2D vortices. The vortex avalanches were also observed at low temperatures in the (Ba,K)Fe_2As_2 crystal. It is proposed that it is the K substitution that induces both almost isotropic superconductivity and the very strong intrinsic pinning in the (Ba,K)Fe_2As_2 crystal.

DOI: 10.1103/PhysRevB.82.024525 PACS number(s): 74.70.Xa, 74.25.F−, 74.25.Wx

A high critical current density, J_c, upper critical field, B_{c2}, and irreversibility field, B_{irr}, a high superconducting transition temperature, T_c, strong magnetic-flux pinning, good grain connectivity, and isotropic superconductivity are the major physical requirements for superconducting materials used in practical applications operating at low and, in particular, high magnetic fields. The conventional low-T_c superconductors, where H_{c2} is also small, can only carry large J_c at very low temperatures. The cuprate high-T_c superconductors suffer from poor grain connectivity and easy melting of the vortex lattice, leading to small J_c in high magnetic fields at relatively high temperatures. For MgB_2 superconductor with T_c of 39 K, B_{irr} is far below H_{c2}, and J_c drops quickly with both field and temperature, preventing its use above 20 K. The newly discovered Fe-based superconductors[1–7] show T_c as high as 55 K and B_{c2} above 200 T, in combination with a small anisotropy for $REFeAsO_{1-x}F_x$ (RE-1111 phase, with RE a rare-earth element)[8] and an almost isotropic superconductivity for (Ba,K)Fe_2As_2 (122 phase).[9] These properties make the Fe-based superconductors extremely promising candidates for high magnetic field applications at relatively high temperatures. The current carrying ability of these superconductors at high fields and temperatures is largely determined by the flux-pinning strength and the behavior of the vortex matter. Therefore, the determination of their intrinsic vortex pinning strength is a central issue from both an applied and a fundamental perspective. Both 1111 and 122 phase compounds have typical two-dimensional (2D) crystal structures. In RE-1111 phase, where RE is a rare-earth element, the FeAs superconducting layers are separated by insulating LaO layers[10] while in Ba(K)-122 phase, the FeAs layer is sandwiched between conductive Ba layers.[5] It is expected that the 122 phase containing two FeAs layers would have small anisotropy and thus higher intrinsic pinning compared to the single layer 1111 phase. Co-doped $BaFe_2As_2$ single crystal shows an anisotropy of 1–3 and upper critical-field values of $B_{c2}(B\|ab)=20$ T and $B_{c2}(B\|c)=10$ T at 20 K, with $dB_{c2}/dT\approx 5$ T/K.[11] For single crystals of the optimally doped $Ba(Fe_{1-x}Co_x)_2As_2$ with $x=0.074$ and critical temperature $T_c\approx 23$ K, the anisotropy of the upper critical field, $\gamma=B_{c2}^{ab}/B_{c2}^{c}$, is in the range of 2.1–2.6, and the critical current density, J_c, is over 10^5 A/cm^2 and 3×10^5 A/cm^2 at 5 K for $B\|ab$ and $B\|c$, respectively.[11] The B_{c2} of $(Ba_{0.55}K_{0.45})Fe_2As_2$ measured under pulsed magnetic fields exceeds 60 T at 14 K.[9] The anisotropy of B_{c2} is moderate (~3.5 close to T_c), and it drops with decreasing temperature, becoming isotropic at low temperatures.[9] Underdoped $BaFe_2As_2$ with T_c of 25 K shows an anisotropy of 3–4.[12]

Another important issue for practical applications is the occurrence of magnetic-flux jumps, which generally occur in larger samples with high critical current densities. Magnetic-flux jumps have been observed in thin-film forms of some type II superconductors, such as Nb_3Sn (Ref. 13) and MgB_2.[14] However, flux jumps have not yet been reported in any Fe-based superconductors so far.

In this paper, we report that the vortex lattice in (Ba,K)Fe_2As_2 crystals appears to be quite rigid, with pinning potentials as high as 10^4 K which show only weak-field dependences up to 10 T. The rigid three-dimensional (3D) vortex lattice in the two-dimensional (Ba,K)Fe_2As_2 seems to differ from the two-dimensional high-T_c cuprate superconductors with their more 2D pancakelike vortex lattices. Flux jumps were observed in one of our large samples at low temperature. The very strong intrinsic supercurrent carrying ability and flux pinning observed in the (Ba,K)Fe_2As_2 superconducting single crystals make this compound very promising for future applications in high magnetic fields.

The 122 crystals used in the present work was grown

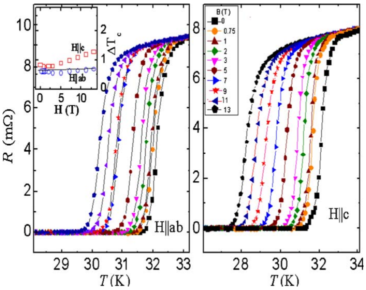

FIG. 1. (Color online) Temperature dependence of the resistance of a $Ba_{0.72}K_{0.28}Fe_2As_2$ crystal measured for $H \| ab$ and $H \| c$ in different magnetic fields, $0 \leq H \leq 13$ T. Inset in the left panel shows the transition width as a function of magnetic field for both directions of applied field.

using a flux method. High purity elemental Ba, K, Fe, As, and Sn were mixed in a mol ratio of $(Ba_{1-x}K_xFe_2As_2)$:Sn $=1:45-50$ for the self-flux. A crucible with a lid was used to minimize the evaporation loss of K as well as that of As during growth. The crucible was sealed in a quartz ampoule filled with Ar and loaded into a box furnace. The details of the crystal growth are given in Ref. 15.

The electrical resistance R versus temperature curves of a $Ba_{0.72}K_{0.28}Fe_2As_2$ crystal for magnetic fields up to 13 T, applied parallel to the *ab* plane and to the *c* axis, are shown in Fig. 1. The resistance starts to drop toward zero at $T=31.7$ K in zero magnetic field, indicating that the crystal is not optimally doped.[16] It can be seen that the onset of T_c decreases with increasing magnetic field very similar to $T_c(R=0)$, such that the transition width ΔT_c remains almost constant for both $B \| ab$ and $B \| c$ [see the inset in Fig. 1(a)]. When the field changes from 0 up to 13 T, the shape of $R(T)$ changes very little. This behavior is reminiscent of the magnetotransport behavior of conventional low-T_c superconductors and significantly different from that of cuprate high-T_c superconductors. In cuprate high-T_c superconductors, the T_c onset temperature does not change much but the $T_c(R=0)$ shifts to low temperature very quickly with field. The field-independent transition width ΔT_c is also quite different from what is observed in $NdFeAs_{0.2}OF_{0.8}$ single crystals, which show a broadening of $T_c(R=0)$ as the field increases.[8] In the following we define the temperature-dependent upper critical field $B_{c2}(T)$ by $R(T,B_{c2})=0.9R_n$, where R_n is the normal-state resistance just above the onset of T_c. In a similar way we define the irreversibility field $B_{irr}(T)$ by $R(T,B_{irr})=0.1\ R_n$. The B_{c2} and B_{irr} obtained for both $B \| ab$ and $B \| c$ are denoted as B_{c2}^{ab}, B_{c2}^{c}, B_{irr}^{ab}, and B_{irr}^{c}, respectively.

It can be seen from Fig. 2 that the B_{c2} values for the $(BaK)Fe_2As_2$ are quite large ($B_{c2}^{ab}=13$ T at 30.7 K and $B_{c2}^{c}=13$ T at 29 K). The slope dB_{c2}/dT is -7.5 and -4.4 for the *ab* and the *c* directions, respectively, for our $Ba_{0.72}K_{0.28}Fe_2As_2$ crystal. From Fig. 2, one can see that B_{irr} is very close to B_{c2} in both field directions, indicating that flux lattice melting in our the $(Ba,K)Ba_2As_2$ crystals seems to occur only over a relatively small area of the *B*-*T* phase diagram.

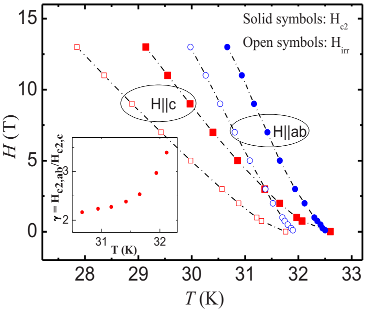

FIG. 2. (Color online) H_{c2} and H_{irr} for both $H \| ab$ and $H \| c$ as a function of temperature. Inset: the anisotropy γ (H_{c2}^{ab}/H_{c2}^{c}) as a function of temperature.

The $B_{c2}(0)$ was estimated by using the Werthamer-Helfand-Hohenberg formula,[17] i.e., $B_{c2}(0)=-0.69\ T_c(dB_{c2}/dT)$, with dB_{c2}/dT at $T=T_c$. We find $B_{c2}^{ab}(0)=170$ T and $B_{c2}^{c}(0)=100$ T for our $(Ba,K)Fe_2As_2$ crystal. Furthermore, one can estimate $B_{c2}(0)$ from $B_{c2}(T)=B_{c2}(0)(1-t^2)/(1+t^2)$, where $t=T/T_c$ which results from the Ginzburg-Landau theory. One finds $B_{c2}^{ab}(0)=195$ T and $H_{c2}^{c}(0)=110$ T. The anisotropy $\gamma=B_{c2}^{ab}/B_{c2}^{c}$ of the 122 crystal was determined to be 2–3.5 for $T>30.5$ K, as can be seen in the inset of Fig. 2. The observed increase in γ with temperature T is opposite to that of Sm-1111 (Ref. 18) and MgB_2 (Ref. 19) superconductors, which might be due to multiband effects in 122 crystals.

According to the thermally activated flux flow model, the temperature and field dependence of the resistivity $R(T,B)$ is described by the equation $R(T,B)=R_0 \exp[-U(T,B)/k_BT]$, where R_0 is a parameter, k_B the Boltzmann's constant, and $U(T,B)$ is the activation energy for vortex bundle hopping, and we assume here $U(T,B)=U_0(B)(1-t)$. In the following we call U_0 the pinning potential. This pinning potential can be obtained from the slope of an Arrhenius plot, $\ln R(T,B)$ versus $1/T$. In Fig. 3, we have plotted the data as $\ln R$ vs $1/T$. The best fit to the experimental data yields values for the pinning potentials of $U_0=9100$ and 5900 K for $B \| ab$ and $B \| c$, respectively, at the low field of 0.1 T. These values are much higher than the reported values of $U_0=2000-3000$ K for $NdO_{0.82}F_{0.18}FeAs$ single crystals.[8] For comparison, we also include U_0 values for Bi-2212 (Ref. 20)

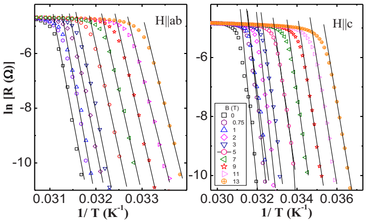

FIG. 3. (Color online) Natural logarithm of the resistance versus $1/T$ for field parallel (left) and perpendicular (right) to the *ab* direction.

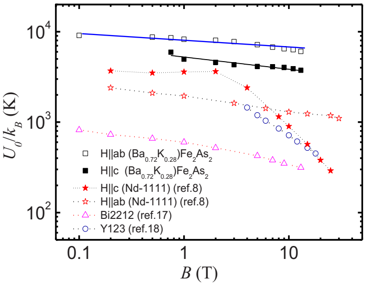

FIG. 4. (Color online) Field dependence of $U_0(B)$ for $Ba_{0.72}K_{0.28}Fe_2As_2$ crystal $(BaK)Fe_2As_2$.

and Y-123 (Ref. 21) single crystals in Fig. 4, even though their T_c's are different.

It has been reported that the pinning potential of bismuth strontium calcium copper oxide (BSCCO) crystals exhibits a power-law dependence on magnetic field, $U_0(B) \propto B^{-n}$, with $n=1/2$ for $B<5$ T and $n=1/6$ for $B>5$ T for $B \| c$.[20,22] However, for the $(BaK)Fe_2As_2$ crystal, U_0 drops very slowly with field as $B^{-0.09}$ and $B^{-0.13}$ for $B \| ab$ and $B \| c$, respectively (Fig. 4). This means that U_0 is almost field independent, which is a remarkable result. The values of U_0 for $(Ba,K)Fe_2As_2$ are three to four times larger than that of Bi-2212 (Ref. 21) and about ten times larger than that of Bi-2223 (Ref. 17) crystals. These values are also more than three times larger than those for $NdO_{0.82}F_{0.18}FeAs$ crystals.[8] Also, the U_0 for our $(Ba,K)Ba_2As_2$ crystal is about one order of magnitude higher than that of Y-123 crystals for fields above 1 T.[18] Thus the value of $U_0(B)$ of our $(Ba,K)Fe_2As_2$ single crystal is of record high compared to any other superconductor in single-crystal form.

It should be noted that the pinning potential of the $(BaK)Fe_2As_2$ crystal is almost field independent for the field range we have measured from 0 up to 13.5 T. However, it is expected that the U_0 should behave differently with field for higher fields, in particularly, for fields close to H_{c2}. Further study on the U_0 for the doped $BaFe_2As_2$ in higher fields is necessary.

A small $(Ba,K)Fe_2As_2$ single crystal in the shape of a long thin strip, obtained by cleaving along the *ab* plane, was investigated using magneto-optical imaging. The left inset in Fig. 5 is a magneto-optical image of the flux penetration into the sample, which was collected while applying a perpendicular field of 50 mT at 20 K. It is evident that the sample is of high uniformity, i.e., without any microcracks or weak links perturbing the flow pattern of the shielding current. Such regular flux patterns allow precise measurements of the critical current density J_c using the Bean critical state model formula for partial penetration in long thin strip geometry[23]

$$\cosh(\pi H/J_c d) = w/(w-2a),$$

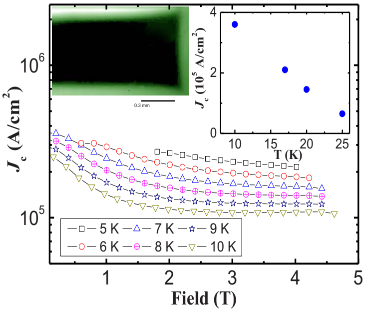

FIG. 5. (Color online) The J_c-field dependence obtained from the *M-H* loops (Fig. 6) measured on a large $Ba_{0.72}K_{0.28}Fe_2As_2$ crystal. Left inset: magneto-optical image of the flux penetration into the right half of the crystal. Right inset: critical current density versus temperature of a small $(Ba,K)Fe_2As_2$ single crystal shaped as a thin rectangular bar at $B=50$ mT.

where *a* is the advancement of the flux front into the strip at an applied field *H*, and *w* and *d* are the width and thickness of the strip, respectively. The obtained values for J_c in the temperature range 10–25 K are plotted in the right inset of Fig. 5.

Magnetization loops (Fig. 6) were collected for a relatively large $(Ba,K)Fe_2As_2$ single crystal ($4.2 \times 2.85 \times 0.15$ mm^3) at different fields $B \| c$ and temperatures down to 5 K. The J_c was obtained from the width ΔM of the magnetization loop using the Bean model, where for full sample penetration

$$J_c = 20\Delta\tilde{M}w(1-\tilde{w}3l).$$

Here *l* is the length of the sample. The resulting J_c versus applied field is plotted in Fig. 5.

For $B<4.5$ T and $T<10$ K the J_c is larger than 10^5 A/cm^2. The slow decrease in J_c with increasing field seems to correlate with the weak-field dependence of the pinning potential U_0. At 5 K, the J_c value is 2.7×10^5 A/cm^2 at $B=2$ T, and it only decreases to 2.2×10^5 A/cm^2 at $B=4$ T. The weak dependence of J_c on magnetic field and temperature suggests that the $(Ba,K)Fe_2As_2$ single-crystal superconductor has a superior

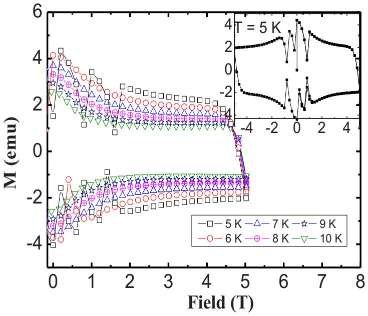

FIG. 6. (Color online) Magnetic hysteresis of a large $Ba_{0.72}K_{0.28}Fe_2As_2$ crystal. Inset shows a full loop at 5 K.

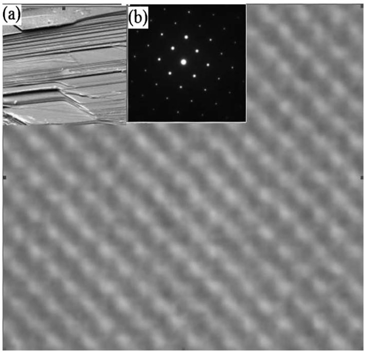

FIG. 7. High-resolution TEM image of a $Ba_{0.72}K_{0.28}Fe_2As_2$ crystal. The insets contain (a) a SEM image of the crystal surface and (b) an electron-diffraction pattern along the (001) direction.

J_c behavior, which is beneficial for potential applications in high magnetic fields.

In general, flux jumps can be observed in magnetization loop measurements of type II superconductors if the following criteria are fulfilled: (a) the sample is sufficiently large, (b) the J_c is sufficiently high, (c) the sample specific heat is small, and (d) the ramp rate of the magnetic field is sufficiently fast. As shown in Fig. 6, we have observed flux jumps in our large $(Ba,K)Fe_2As_2$ single crystals at temperatures below 7 K. The shapes of these magnetization jumps are very similar to the ones that have previously been observed and modeled in melt-textured YBCO samples.[24] So far, the occurrence of flux jumps has not been reported in any of the Fe-based superconductors.

Scanning electron microscopy (SEM) revealed that the 122 crystal has a typical 2D crystal structure [inset (a) in Fig. 7]. According to our transmission electron microscopy examination, we did not observe any noticeable crystal defects which could be possible pinning centers for the vortices. One of the typical atomic images taken along the [001] direction is presented in Fig. 7, which shows the typical features of square lattices on the (110) plane. All the surface atoms are perfectly ordered, and no superstructures are observed, as indicated by the selected large area electron-diffraction pattern [inset (b) in Fig. 7]. These results reveal that the 122 crystal has a very high crystallinity. Usually, the pinning is weak in a superconducting crystal with very high crystallinity. Here the question arises where the strong pinning comes from in a perfect 122 crystal. There are two possible causes one might think of. First, the K doping turns the parent compound from being nonsuperconducting into superconducting and at the same time introduces imperfections into the crystal lattice due to its different ionic size compared to Ba^{2+}. These lattice imperfections may act as intrinsic pinning centers in the $(Ba,K)Fe_2As_2$. Second, it has been reported that for the Fe-based superconductors, superconducting gaps vary with the characteristic length scales of the deviations from the average gap value.[25] These variations in the gap magnitude, the zero-bias conductance, and the coherence peak strength are quite well matched to each other. Moreover, these are further correlated with the average separation between the K dopant ions in the superconducting FeAs planes for the $(Ba,K)Fe_2As_2$ crystal, which implies that the strength of the superconductivity is not uniform throughout the FeAs planes. The inhomogeneous superconducting strength may act as a source of pinning centers once magnetic flux exists inside the superconductor.

The nearly isotropic superconductivity[9] as indicated in the inset of Fig. 2, correlates well with the observed large critical current densities and large U_0 values in our $(Ba,K)Fe_2As_2$ single crystals. In $NdO_{0.82}F_{0.18}FeAs$ the pinning potential was found to be smaller, $U_0=2000-3000$ K.[8] This might be understood in terms of the stronger superconducting coupling between the FeAs superconducting layers in the FeAs-122 phase compared to the FeAs-1111 phase. In the FeAs-122 phase, there are two superconducting FeAs layers, and the coupling between the superconducting layers is stronger than in the FeAs-1111 phase, which results in nearly isotropic superconductivity as well as in a more 3D vortex lattice. That is to say, despite of the two-dimensional nature of crystal structure of the 122 phase, the vortex lattice can still be easily pinned by any pinning centers. Thus $(Ba,K)Fe_2As_2$ single crystals have the ability to carry large supercurrents in high magnetic fields. The 3D-like vortex lattice in $(Ba,K)Fe_2As_2$ single crystals distinguishes this compound from high-T_c cuprate superconductors such as BSCCO where layers of 2D pancake vortex lattices interact relatively weakly with each other.

In conclusion, we found that the $(Ba,K)Fe_2As_2$ crystal shows very high intrinsic flux-pinning strength, almost field independent high values of critical current density, high pinning potential of 10^4 K, high H_{c2}, high H_{irr}, and low values of anisotropy of 1–3. The obtained U_0 values are record high compared to any existing superconducting single crystal. The isotropic rigid vortices observed in the two-dimensional $(Ba,K)Fe_2As_2$ distinguish this compound from 2D high-T_c cuprate superconductors with 2D vortices. We observed the vortex avalanches in $(Ba,K)Fe_2As_2$ due to high J_c which further supports the high value of the pinning potential and the intrinsic strong flux pinning in this compound. It is the K substitution that induces both isotropic superconductivity and the very strong intrinsic pinning in the 122 compounds. The very strong intrinsic supercurrent carrying ability and flux pinning observed in the $(Ba,K)Fe_2As_2$ superconducting single crystals make this compound very promising for future applications in high magnetic fields.

X.L.W. is thankful for the support by the Australian Research Council through ARC Discovery Projects No. DP1094073 and No. DP0558753, and the support by MIST/KRF (Grant No. 2009-0051705) of Korea.

*Author to whom correspondence should be addressed; xiaolin@uow.edu.au

†Deceased.

[1] Y. Kamihara, T. Watanabe, M. Hirano, and H. Hosono, J. Am. Chem. Soc. **130**, 3296 (2008).

[2] X. H. Chen, T. Wu, G. Wu, R. H. Liu, H. Chen, and D. F. Fang, Nature (London) **453**, 761 (2008).

[3] Z. A. Ren, J. Yang, W. Lu, W. Yi, X.-L. Shen, Z.-C. Li, G.-C. Che, X.-L. Dong, L.-L. Sun, F. Zhou, and Z.-X. Zhao, EPL **82**, 57002 (2008).

[4] C. Wang, L. Li, S. Chi, Z. Zhu, Z. Ren, Y. Li, Y. Wang, X. Lin, Y. Luo, S. Jiang, X. Xu, G. Cao, and Z. Xu, EPL **83**, 67006 (2008).

[5] M. Rotter, M. Tegel, and D. Johrendt, Phys. Rev. Lett. **101**, 107006 (2008); K. Sasmal, B. Lv, B. Lorenz, A. M. Guloy, F. Chen, Y.-Y. Xue, and C.-W. Chu, *ibid.* **101**, 107007 (2008).

[6] N. Ni, S. L. Bud'ko, A. Kreyssig, S. Nandi, G. E. Rustan, A. I. Goldman, S. Gupta, J. D. Corbett, A. Kracher, and P. C. Canfield, Phys. Rev. B **78**, 014507 (2008).

[7] X. L. Wang, S. R. Ghorbani, G. Peleckis, and S. Dou, Adv. Mater. **21**, 236 (2009).

[8] J. Jaroszynski, F. Hunte, L. Balicas, Y.-j. Jo, I. Raičević, A. Gurevich, D. C. Larbalestier, F. F. Balakirev, L. Fang, P. Cheng, Y. Jia, and H. H. Wen, Phys. Rev. B **78**, 174523 (2008).

[9] H. Q. Yuan, J. Singleton, F. F. Balakirev, S. A. Baily, G. F. Chen, J. L. Luo, and N. L. Wang, Nature (London) **457**, 565 (2009).

[10] F. Hunte, J. Jaroszynski, A. Gurevich, D. C. Larbalestier, R. Jin, A. S. Sefat, M. A. McGuire, B. C. Sales, D. K. Christen, and D. Mandrus, Nature (London) **453**, 903 (2008).

[11] N. Ni, M. E. Tillman, J.-Q. Yan, A. Kracher, S. T. Hannahs, S. L. Bud'ko, and P. C. Canfield, Phys. Rev. B **78**, 214515 (2008).

[12] H.-J. Kim, Y. Liu, Y. S. Oh, S. Khim, I. Kim, G. R. Stewart, and K. H. Kim, Phys. Rev. B **79**, 014514 (2009).

[13] I. A. Rudnev, S. V. Antonenko, D. V. Shantsev, T. H. Johansen, and A. E. Primenko, Cryogenics **43**, 663 (2003).

[14] T. H. Johansen, M. Baziljevich, D. V. Shantsev, P. E. Goa, Y. M. Gal pe rin, W. N. Kang, H. J. Kim, E. M. Choi, M.-S. Kim, and S. I. Lee, Europhys. Lett. **59**, 599 (2002).

[15] G. L. Sun, D. L. Sun, M. Konuma, P. Popovich, A. Boris, J. B. Peng, K.-Y. Choi, P. Lemmens, and C. T. Lin, arXiv:0901.2728 (unpublished).

[16] H. Chen, Y. Ren, Y. Qiu, W. Bao, R. H. Liu, G. Wu, T. Wu, Y. L. Xie, X. F. Wang, Q. Huang, and X. H. Chen, EPL **85**, 17006 (2009).

[17] N. R. Werthamer, E. Helfant, and P. C. Hohenberg, Phys. Rev. **147**, 295 (1966).

[18] S. Weyeneth, R. Puzniak, U. Mosele, N. D. Zhigadlo, S. Katrych, Z. Bukowski, J. Karpinski, S. Kohout, J. Roos, and H. Keller, J. Supercond. Novel Magn. **22**, 325 (2009); L. Balicas *et al.*, arXiv:0809.4223 (unpublished).

[19] M. Angst, R. Puzniak, A. Wisniewski, J. Jun, S. M. Kazakov, J. Karpinski, J. Roos, and H. Keller, Phys. Rev. Lett. **88**, 167004 (2002); L. Lyard, P. Samuely, P. Szabo, T. Klein, C. Marcenat, L. Paulius, K. H. P. Kim, C. U. Jung, H.-S. Lee, B. Kang, S. Choi, S.-I. Lee, J. Marcus, S. Blanchard, A. G. M. Jansen, U. Welp, G. Karapetrov, and W. K. Kwok, Phys. Rev. B **66**,180502(R) (2002).

[20] T. T. M. Palstra, B. Batlogg, R. B. van Dover, L. F. Schneemeyer, and J. V. Waszczak, Phys. Rev. B **41**, 6621 (1990).

[21] D. López, L. Krusin-Elbaum, H. Safar, E. Righi, F. de la Cruz, S. Grigera, C. Feild, W. K. Kwok, L. Paulius, and G. W. Crabtree, Phys. Rev. Lett. **80**, 1070 (1998).

[22] X. L. Wang, A. H. Li, S. Yu, S. Ooi, K. Hirata, C. T. Lin, E. W. Collings, M. D. Sumption, M. Bhatia, S. Y. Ding, and S. X. Dou, J. Appl. Phys. **97**, 10B114 (2005).

[23] E. H. Brandt and M. Indenbom, Phys. Rev. B **48**, 12893 (1993).

[24] K.-H. Müller and C. Andrikidis, Phys. Rev. B **49**, 1294 (1994).

[25] Y. Yin, M. Zech, T. L. Williams, X. F. Wang, G. Wu, X. H. Chen, and J. E. Hoffman, Phys. Rev. Lett. **102**, 097002 (2009).